Modeling Studies of Photoionization Experiments Driven by Z-pinch X-rays

Senior Thesis in Astrophysics

Department of Physics and Astronomy

Swarthmore College

500 College Avenue

Swarthmore, PA 19081

Nathan C. Shupe

nshupe1@swarthmore.edu

March 16, 2005

Advisor: David H. Cohen

ABSTRACT

We have conducted modeling studies of several gas cell shots on the Z accelerator at Sandia National Laboratories in order to study the effects of the irradiance of a low-density gas by a strong x-ray source. Thus far, we have successfully matched a synthesized neon absorption spectrum to an experimental spectrum obtained from one of the shots, with especially good agreement for many of the He-like neon absorption lines. We have also conducted a study scaling the density of the Ne in the gas cell, and have concluded that the minimum density for which there are still measurable spectral features is on the order of $\sim 7.5 \times 10^{16}$ cm^{-3}, which implies an ionization parameter of ~ 70 erg cm s^{-1}. Lastly, we have synthesized new spectral diagnostics for future experiments in the form of time-resolved absorption and emission spectra, and predict that future experiments using such diagnostics will show the weakening of Li-like lines in both absorption and emission and the strengthening of the Lyman alpha line in emission as time progresses. These results have demonstrated we can successfully model the photoionization experiments being conducted at Sandia, and that our modeling procedure can be implemented to design new experiments for future shots at Sandia. Our analysis of the excitation/ionization kinematics and physical conditions of the photoionized plasma has also helped benchmark the atomic kinetics models for these plasmas, which should lead to better interpretation of measured spectra from plasmas photoionized by cosmic sources.

1. Introduction

1.1. Types of astrophysical objects

Photoionized plasmas are characteristic of some of the brightest x-ray sources in the sky, including but not limited to black hole and neutron star binaries (x-ray binaries) and active galactic nuclei (quasars). In a x-ray binary system (XRB), the compact object (a black hole or neutron star) can capture some of the material released in the stellar wind of a nearby giant star. An artist's conception of such a system in shown in Fig. 1.1. As the material spirals toward the compact object, its gravitational energy is converted to thermal kinetic energy. Hard (high-energy) x-rays generated in the accretion disk photoionize the nearby cool circumstellar gas and produce radiation in the form of radiative recombination continua and recombination cascades (4).

In 1999, the launch of the National Aeronautics and Space Administration's *Chandra* and the European Space Agency's *XMM-Newton* x-ray telescopes made available to the scientific community for the first time new high-resolution spectroscopy of astrophysical phenomena. The advent of these telescopes and their accompanying high resolution spectroscopy has fueled the demand for a high degree of accuracy in our spectral models. Much work already has been done in developing spectral models for coronal plasmas, while significantly less work has been devoted to the development of spectral models for photoionized plasmas (2). The apparent lack of well tested spectral models for photoionized plasmas means that at present we cannot be certain of the accuracy of our interpretation of the spectra from these sources. Therefore, until we benchmark and test our spectral models for photoionized plasmas, many of the brightest cosmic x-ray sources will continue to be unavailable for detailed and accurate spectroscopic investigations.

1.2. Differences between photoionized spectrum and coronal spectrum

The two main classes of x-ray sources differ mostly in the process that dominates excitation, de-excitation, and ionization for each. A collisionally dominated (or coronal) plasma is so named because collisions are the driving force of heating in the plasma. Electron impacts with ions populate excited levels and electron-ion collisions are the main source of ionization. The equation of ionization equilibrium for a collisionally dominated plasma can be written as an equivalence between the ionization processes and the recombination processes:

$$n_e C_i n_i = n_e \alpha_{i+1} n_{i+1}, \tag{1.1}$$

where n_e (cm^{-3}) is the electron number density, n_i is the number density of ions of charge state i, n_{i+1} is the number density of ions of charge state $i+1$, C_i (cm^3 s^{-1}) is the collisional
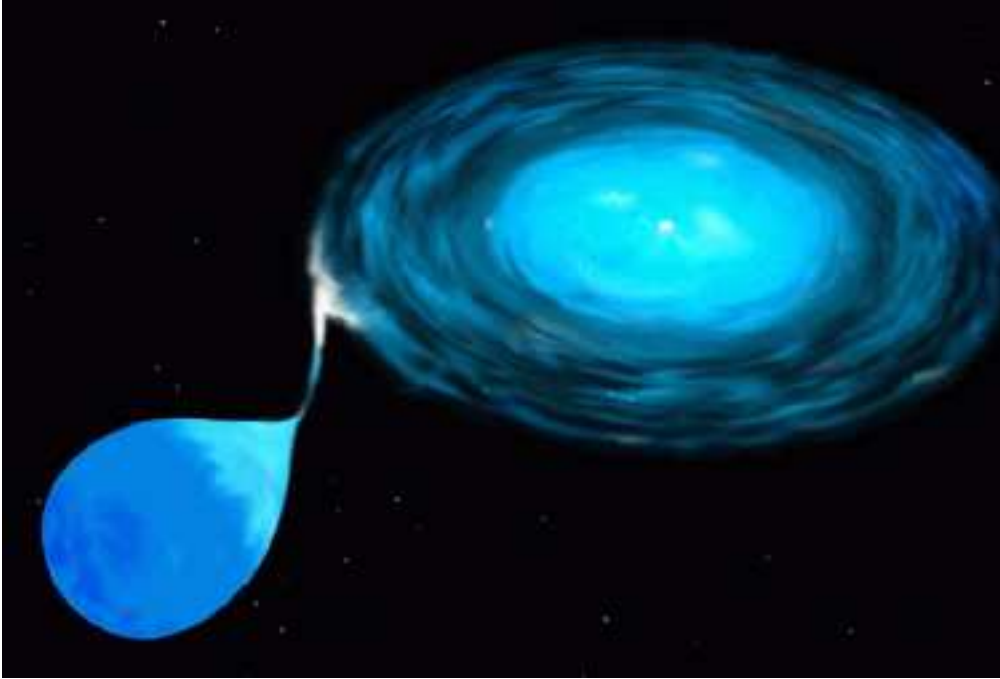
Fig. 1.1.— An artist conception of an x-ray binary. Pictured is a compact object gravitationally capturing wind material from a nearby blue giant star. This captured wind material spirals toward the compact object and forms an accretion disk. The inner parts of this accretion disk are extremely hot and emit continuum radiation in the x-ray band of the electromagnetic spectrum. Image Credit: Space Telescope Science Institute, NASA.

ionization rate for ions with charge state i, and α_{i+1} (cm^3 s^{-1}) is the recombination rate (for both dielectronic and radiative recombination) for ions with charge state $i+1$. Solving for the ionization balance, $\frac{n_{i+1}}{n_i}$, we find that it is completely determined by the ratio of the *temperature* dependent rates C_i and α_{i+1}. Thus, the temperature sets the ionization balance in a coronal plasma, and for an x-ray emitting plasma is of order several hundred eV (similar to the ionization potential of the atoms in the plasma).

The temperature, however, is not the only independent variable that sets the ionization balance of a photoionized plasma. For this type of plasma, we find that there is a new term on the left side of the ionization equilibrium equation which takes into account the photoionization processes and is dependent on the ionizing flux of radiation. Thus, in these plasmas, ionization is driven both by electron temperature and by an ionizing flux of radiation. As a result, in a photoionized plasma it is possible to achieve the same degree of ionization as a coronal plasma with a lower electron temperature. The degree to which the plasma is *overionized* relative to its electron temperature is fully determined by the ionization parameter,

ξ, which we will define and derive in Section 1.6.

As one might expect, the spectra obtained from these two classes of plasma have distinct differing features. Since x-ray coronal plasmas are at higher temperatures, ionization is primarily balanced by dielectronic recombination (excess energy of the recombined electron is used to excite another ionic electron, making the ion doubly-excited), while the cooler photoionized plasmas balance ionization with radiative recombination (excess energy of the recombined electron is radiated away) and cascade following recombination (4). An example spectrum of a x-ray photoionized source is shown in Fig. 1.2, and a zoomed in view of a radiative recombination continua feature in this spectrum is shown in Fig. 1.3.

Shown in Fig. 1.4 are model emission rate spectra for a coronal and a photoionized plasma. Notice that certain line features of the coronal spectrum are not present in the photoionized spectrum. Since the processes governing electronic transitions and ionization differ between the two classes, any spectral model of an x-ray source should employ an atomic model specific to the class of that source. That is, even if we have well-developed atomic models for one class of x-ray source (as we do for coronal plasmas), we cannot apply these models to interpret spectra from sources of the other class (in this case, photoionized plasmas) and expect a high degree of accuracy. If we desire accurate interpretation of x-ray spectra then we require an accurate spectral model for each class of sources.
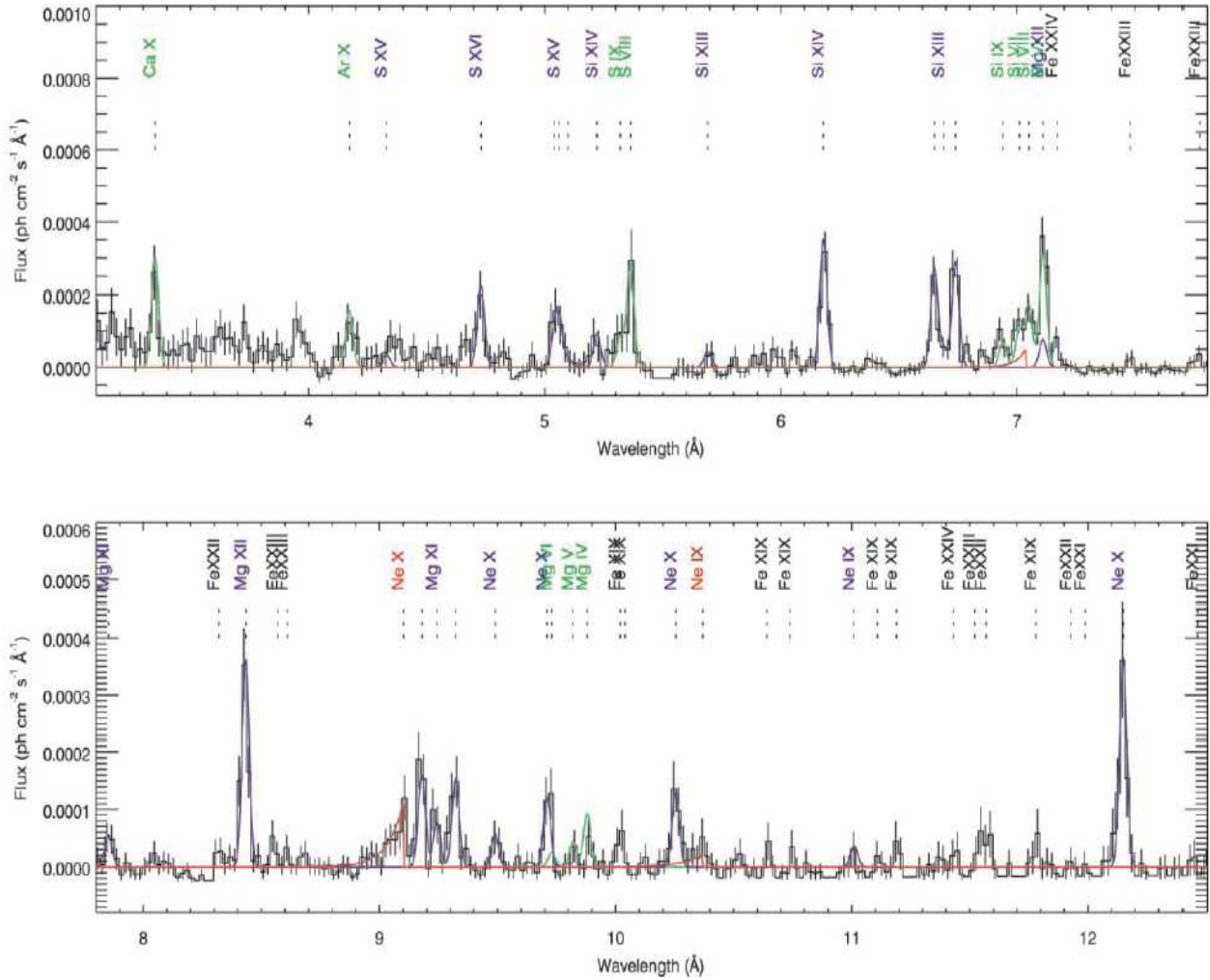
Fig. 1.2.— A high-resolution x-ray spectrum of the ionized stellar wind of Vela X-1 during eclipse captured with the High-Energy Transmission Grating Spectrometer (HETGS) on board the Chandra X-ray Observatory. The fluorescent lines are plotted in green, the highly ionized lines in blue, and the radiative recombination continua (which are characteristic of a photoionized plasma) in red. Figure taken from (17).
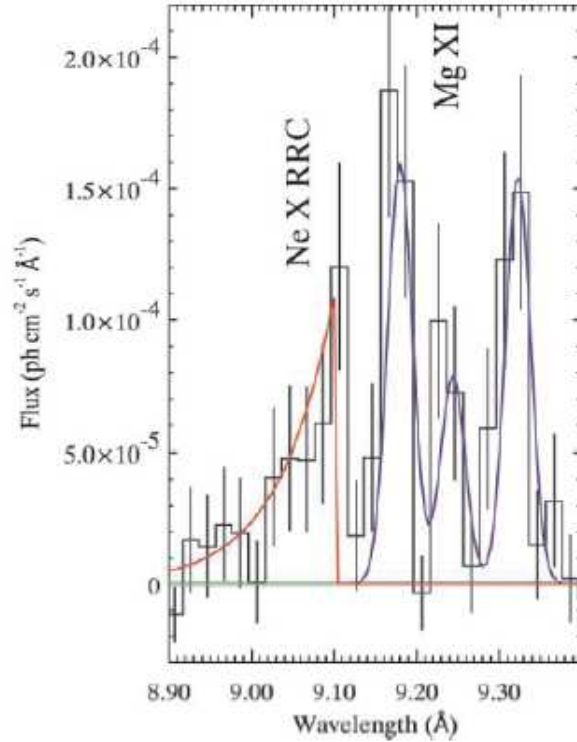
Fig. 1.3.— Shown here is a zoomed in portion of the spectrum displayed in Figure 1.2. One of the emission lines over this wavelength interval is the Ne X radiative recombination continua (RRC) *line*. In truth, this feature is not a line, but instead continuum emission. For energies greater than (or wavelengths shortward of) the recombination edge (the wavelength at which the energy of the emitted photon, E_γ, is exactly equal to the ionization potential of the ion, χ), any and all free electrons may be captured. After the electron has been captured, its excess energy ($E_\gamma = E_e - \chi$) is radiated away. The maximum emission occurs for energies just greater than the ionization potential, since these free electrons have the greatest chance of being captured by the ion. We would also expect the width of the line to depend on temperature, since assuming a Maxwellian distribution of velocities more free electrons will have energies greater than the ionization potential for a higher electron temperature. The functional form of this width dependence on temperature is $\approx kT_e$, so for a photoionized plasma of lower electron temperature (less than the temperature corresponding to the ionization potential), this continuum feature will appear narrow, almost like a line feature. For this reason, photoionized plasmas are said to be characterized by narrow RRC features. Figure taken from (17).
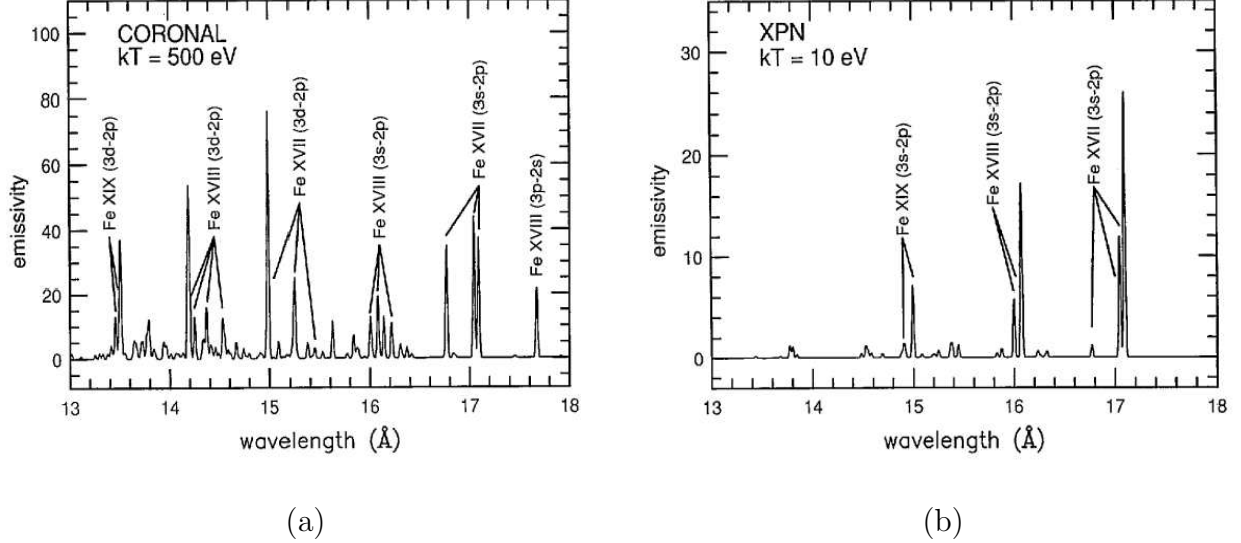
(a) (b)

Fig. 1.4.— Iron model emission rate spectra for (a) a coronal plasma ($kT_e = 500$ eV, $n_e = 10^{11}$ cm^{-3}) and (b) a photoionized plasma ($kT_e = 10$ eV, $n_e = 10^{11}$ cm^{-3}). Important to note is that the plasmas displayed in each frame have the same ionization balance, despite vastly different temperatures. This feature of equivalent ionization balance for a lower temperature is what characterizes photoionized plasmas. Also note the absence of any de-excitations from the $3d$ or $3p$ energy levels to the $2p$ energy level in the photoionized plasma. From this we can conclude that photoionized plasmas are characterized by a different set of spectral signatures than coronal plasmas. Both of these figures are taken from (4).

1.3. Laboratory Experiments

Traditionally, astrophysics has not been included in the category of laboratory sciences. Strictly speaking, this omission from the family of laboratory sciences has been because those objects and phenomena in which astrophysics is interested are accessible only through remote observation. That is, an astronomer does not (and, given our current state of technology, cannot) determine the temperature of a star by getting into a spaceship, flying to the star, and then sticking a big thermometer into its surface. Instead, the astronomer collects light from the star, breaks the light up into its constituent wavelengths to form of a spectrum, and then infers from the shape of the light distribution an approximate temperature for the star.

Of course, we could avoid the accessibility issue if the phenomena we would like to study could be recreated in some comparable form here on our own planet. Unfortunately, since the scales and environments in which astrophysical phenomena occur differ so dramatically from anything we have (until recently) been able to reproduce in the laboratory, the study of these phenomena has generally been limited to observation and computer modeling.[1] That is not to say that observation and computer modeling are not effective procedures, for certainly the opposite is true, but there does exist a problem inherent to these procedures in that the only calibration of the model is the data the model is trying to explain. Essentially this means that models calibrated only by observational data tend to preferentially fit the data from some sources better than from other sources, unless certain parameters in the model are adjustable. Adjustable parameters are not necessarily a bad thing, but they are certainly not welcome in great numbers. Ideally, we would like to have models that minimize the number of adjustable or free parameters, which would indicate that we have sufficiently modeled the physics governing the situation in order to constrain the values for most of the parameters. The more data we acquire from a wide range of types of sources, the easier it is to constrain the number of adjustable parameters. In the case of cosmic sources, however, the variety of sources we can observe is not up to us, sometimes making it difficult to minimize the number of adjustable parameters in our models.

Like observations of cosmic sources, laboratory experiments provide a source of data by which spectral codes can be tested and benchmarked. Unlike observations, however, laboratory experiments provide an environment in which the emitting plasma can be controlled and characterized. That is, in laboratory experiments, we can control what type of gas is irradiated, the position of the gas relative to the x-ray source, and the magnitude of x-rays

---

[1]There have been notable exceptions to this rule, including (but not limited to) the returned lunar samples of the Apollo missions to the moon, objects that have happened to collide with the Earth (meteorites), and as recently as this year the Deep Impact mission to return comet samples to Earth.

which irradiate the gas, while also being able to directly observe the plasma and characterize some of its properties (e.g. temperature, density, velocity). Therefore, the local and more versatile laboratory experiments allow us to more readily benchmark the atomic kinetics models used to interpret the spectra from photoionized plasmas.

While laboratory experiments are useful in that they provide us with a plethora of varied data which allow us to efficiently and effectively calibrate our models, they are not without their inherent drawbacks. In the case of the gas cell experiments, it is difficult to achieve in the laboratory a plasma photoionized to the degree we observe in cosmic phenomena. As will be discussed in Section 1.6, the degree to which a plasma is photoionized depends directly on the luminosity of the ionizing source, and inversely on the distance from the source and the gas plasma density. Assuming a fixed luminosity of the ionizing source in the gas cell experiments, then the magnitude of this *ionization parameter* is determined fully by the radial distance and the density. For the gas cell experimental setup, the flexibility of the radial distance is limited, so to maximize the degree of ionization of the plasma we must minimize the density. Herein is where the problem arises, since for a lower density the line features in the measured spectra will be weaker. Ideally, the cell would be an infinitely long tube filled with low density gas, so that we could maximize the ionization parameter while still measuring strong line features in the spectra. However, given that an infinitely long tube is hard to fit in a finite sized vacuum chamber, we are forced to compromise and choose the minimum density that will provide measurable spectral features. Unfortunately, the ionization parameter corresponding to this density is typically much smaller than the cosmically relevant values, so unless the gas cell can be moved much closer to the x-ray source or the luminosity of the x-ray source can be increased dramatically, the plasmas created in these laboratory gas cell experiments will not be photoionized to the degree we would like.

1.4. Gas cell experiments

A series of ride-along gas cell shots were conducted at the Sandia National Laboratories Z pulsed power accelerator (see Section 1.5 for a description of the facility). The experimental package consists of a cm-scale neon filled cell with mylar windows, mounted several cm from the anode current return can, inside of which lies the Z-pinch. In this configuration, the pinch is analogous to the x-ray emmitting accretion disk in an x-ray binary, and the gas in the cell is like the photoionized circumstellar gas. Experiments already completed have used Ne of density $n_{ion} \sim 10^{18}$ cm^{-3} observed in absorption (the pinch serves as the backlighter) with a time-integrated spectrometer. For future experiments, we plan to make simultaneous time-resolved emission and absorption spectroscopic measurements along the lines of sight pictured in Fig. 1.5.
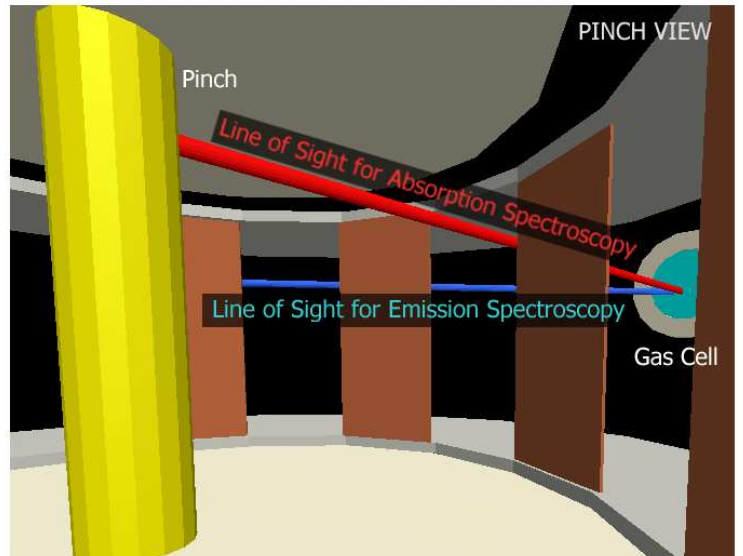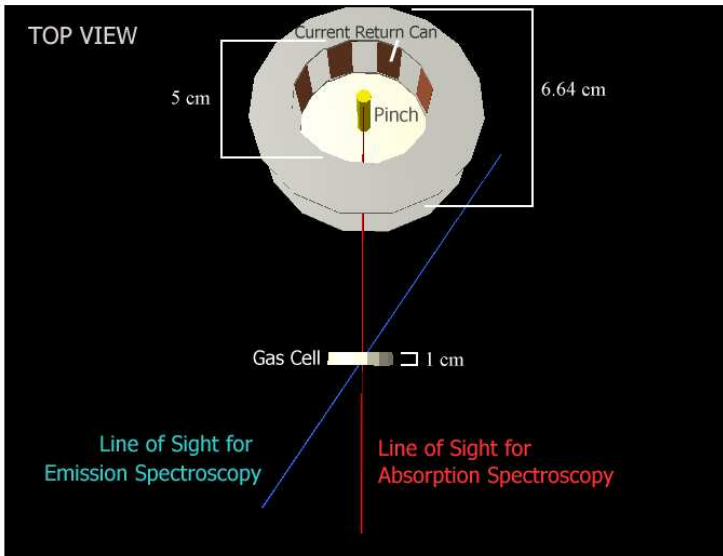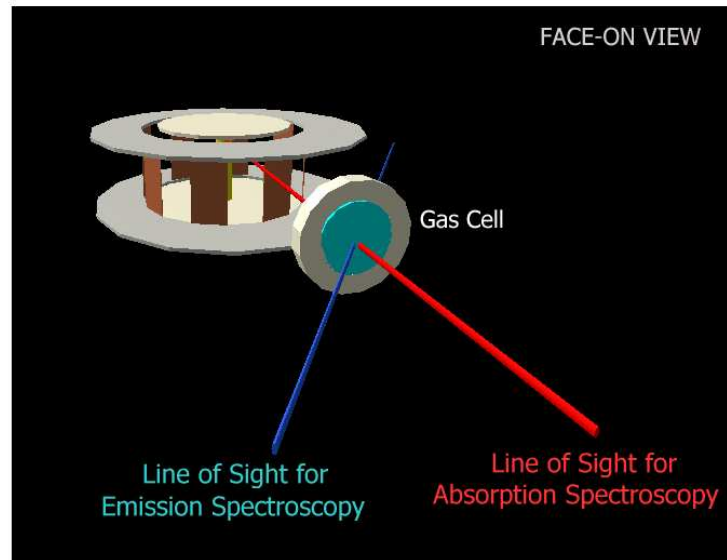
Fig. 1.5.— Face-on, top and pinch views of the experimental set up, with the spectroscopic lines of sight shown in red and blue. Note that the gas in the cell is analogous to the photoionized plasmas in the x-ray binary system.

1.5. Z-pinch and Z-machine

The Z-pinch plasma that emits the x-rays that photoionize the gas in our cell is created in the Z pulsed power accelerator at Sandia National Laboratories in Albuquerque, New Mexico. The Z accelerator is the most powerful source of x-rays in the world, producing an x-ray power in excess of 200 TW for an order 100 ns pulse which amounts to a total of 1.9 MJ for the entire pulse (18). It is also the most efficient x-ray source on Earth, converting greater than 10 percent of its input energy into output radiant x-ray energy (9). See Fig. 1.6 for a photograph of the Z Accelerator at Sandia National Laboratories.
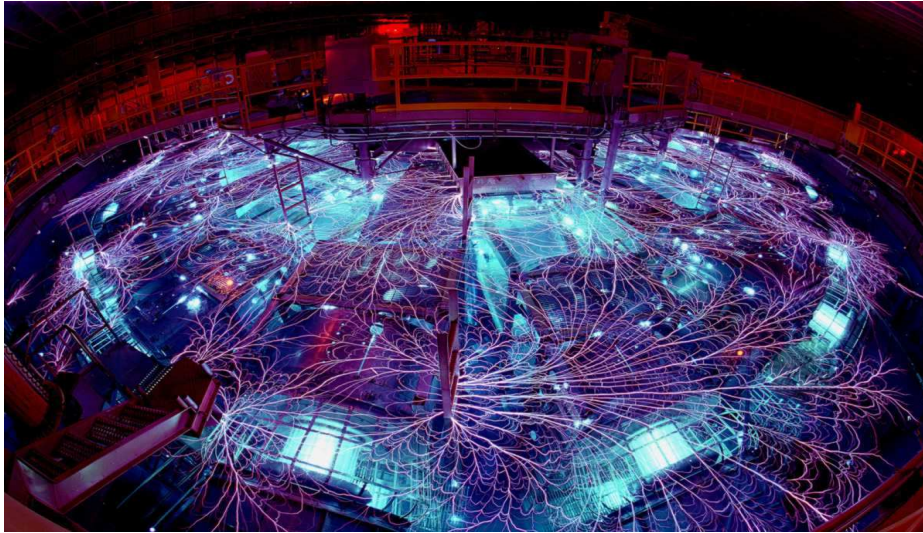

Fig. 1.6.— The Z Accelerator at Sandia National Laboratories. Shown is an extended exposure photograph of the banking of the pulse-forming switches before a shot. The accelerator tank is filled with de-ionized water which acts an insulator for the capacitors lining the edge of the tank. Unfortunately, the de-ionized water is not a perfect insulator, allowing some of the electrical energy stored in the pulse forming switches and transmission lines to leak out into the accelerator tank and produce the flashes of electricity along the surface of the water known as flashover arcs which are not unlike strokes of lighting. To give an indication of size scale, the pulse-forming lines shown glowing blue and rotated about the central axis (like the spokes of a bicycle wheel) in the image, are 30 feet long and have a diameter of several feet.

As a pulsed-power system, the purpose of the Z accelerator is to convert electrical energy at low powers and long timescales to high powers and short timescales, and then deliver that transformed energy to the Z-pinch load. The Z accelerator accomplishes this using a high-voltage Marx generator to charge an intermediate storage capacitor, which forms the pulse to be delivered to the pinch load. The Marx generator is made up of a number of

capacitors lining the rim of the accelerator that are slowly charged in parallel. By utilizing multiple capacitors, this system increases the voltage delivered to the pinch without requiring an increase in storage capacity of any individual capacitor. Once fully charged, the Marx generator slowly (μs timescales) discharges in series to a cylindrical pulse-forming line (PFL) which acts as an intermediate storage capacitor. Once charged to capacity, the pulse forming line is rapidly (ns timescales) discharged into the Z-pinch load.

A cylindrical array of several hundred tungsten wires acts as the Z-pinch load in these experiments. Historically, single wires were the first loads used in pulsed-power systems, but it was found that one could more efficiently create a high density and temperature plasma by converting the kinetic energy of an imploding material after it has stagnated on the z-axis (3). In both cases, a large voltage is applied across the load, inducing a large current in the load. The large current vaporizes the wire (or wires, in the cylindrical array case) and creates a low-resistance plasma capable of carrying a large current. Moving charge induces a magnetic field, which means that a current moving in the negative z direction creates a magnetic field directed in the clockwise direction about the pinch. Using the right-hand rule, we see that for a negative z directed current and a clockwise directed magnetic field, the force on any particle is directed inward toward the central axis of the pinch (see Fig. 1.7). While it is easy to imagine why this is the case for the single wire, it is not so clear why this compression feature would also be characteristic of the wire array. Namely, the individual force vectors due to each differential piece of pinch plasma (except for the piece direcly across from the material in question) either will not point toward the z-axis or they will not be perpendicular to the z-axis. However, all components of the individual force vectors other than those directed toward and perpendicular to the z-axis will cancel with each other due to the symmetry of the system about the z-axis. Thus, for both the single wire and the wire array, the pinch plasma compresses or *pinches* toward the z-axis (hence the names Z-pinch and Z accelerator).

The magnitude of the force on the plasma is quite signficant since the current is of order 10^6 A, so the pinch plasma in the wire array case can be accelerated to a high implosion velocity, of order 10^8 cm s^{-1} (3). By equating kinetic energy to thermal energy for a single particle of mass m_p (mass of a proton), then we can equate this implosion velocity to a final temperature of the pinch: $T \sim 3$ keV.[2] This high implosion velocity is precisely why the wire array system is more effective than the single wire system in creating a high density and high temperature plasma. In order to increase the density and temperature of the plasma

---

[2] While it is quite common to express temperature in units of eV, it should be noted that these are in fact units of energy and not temperature. Throughout the remainder of this paper temperatures are expressed in units of eV such that kT is in units of eV for a given T.
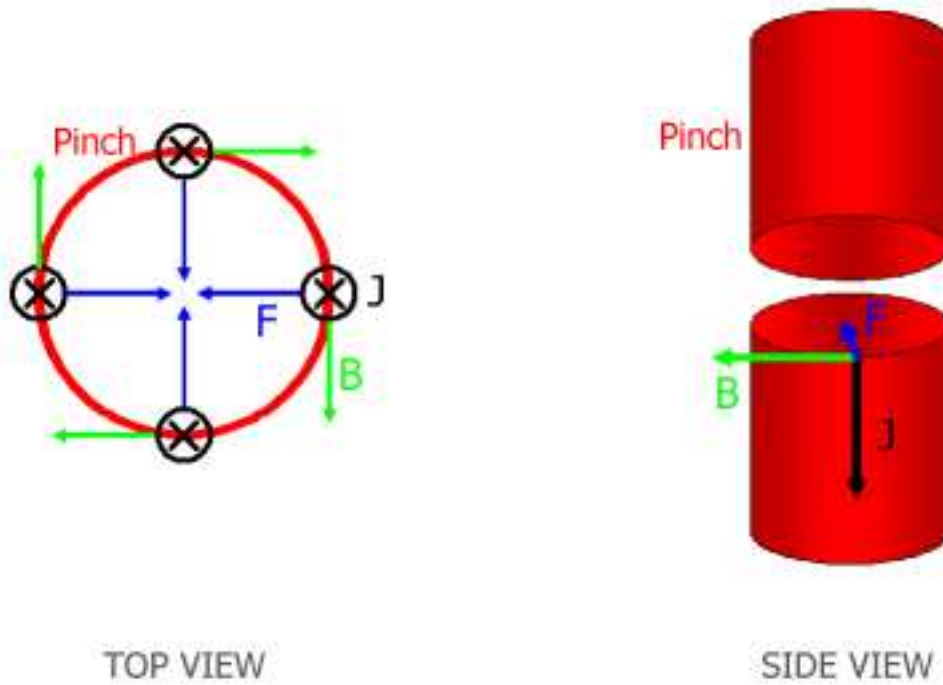
Fig. 1.7.— Schematic drawings of the $\vec{J} \times \vec{B}$ force on pinch plasma particles. Notice that the force vector points radially inward at each point on in the pinch.

produced from the single wire Z-pinch, one can only increase the voltage and power of the pulsed-power system. Using the wire array, however, we are able to increase the strength of the induced magnetic field and thus the implosion velocity and kinetic energy without modifying any parameters of the pulsed-power system. For higher degrees of kinetic energy, more energy is available for conversion when the pinch plasma stagnates on the z-axis, so these plasmas will radiate more x-rays than those with lower kinetic energies.

The Z accelerator is a fast pulsed-power system, delivering its 20 MA current to the load in a short pulse, on the order of 100 ns. This system takes advantage of the feature of pinch plasmas that the plasma will remain stable as long as it has not achieved an equilibrium with the magnetic field. Thus, if one can deliver the electrical energy to the load in a shorter pulse, the pinch plasma will implode faster and the growth of magneto Rayleigh-Taylor instabilities[3] leading up to stagnation on the z axis will be minimized (3). This is precisely

---

[3]Generally speaking, a Rayleigh-Taylor instability is a type of fluid stability that occurs when a heavy

what the Z accelerator does, and explains why this facility is one of the most effective in creating highly radiative Z-pinch plasmas.

1.6. Ionization Parameter

As will be shown in Chapter 2, the modeling work we have done pertains only to the gas cell experiments. Essentially, our work has been to theoretically model an experimental model of the astrophysical sources in which we are interested. While it is our goal to achieve good agreement between our theoretical and experimental models, it is also important that we have a method for checking the agreement between our experimental models and the actual astrophysical sources. Since we are concerned with photoionized astrophysical sources, our procedure of checking agreement would be made quite simple if we had a parameter which characterized the degree of photoionization of a plasma. Then, we could check the value of this parameter for both the gas cell experiments and an astrophysical source, and verify that the two were in relative agreement. Luckily, such a parameter can be defined, and it is called the *ionization parameter*.

For an optically thin environment surrounding a compact x-ray source which is emitting isotropically and homogeneously, we can approximate the radiation field present at radius r as the central source spectrum scaled by geometric dilution. Thus, the flux f received at a location some distance r away from the radiation source is given by the inverse square law,

$$f = L/4\pi r^2 \propto L/r^2, \tag{1.2}$$

where (in cgs units) L is the luminosity in ergs s^{-1}, r is the distance from the source in cm and f is the flux in units of erg s^{-1} cm^{-2}.

The state of the gas is described by its (electron) temperature and by the ion populations. If we fix the temperature of the x-ray source (and, thus, its luminosity if we approximate the source as a blackbody) and choose a value for the electron temperature of the gas, then the ionization equilibrium ratios for different charge states depend only on the ionization parameter, which is defined as

$$\xi(r) \equiv L/nr^2 = 4\pi f/n, \tag{1.3}$$

---

fluid is accelerated by a light fluid. In case of the Z-pinch, these instabilities can form because the lighter outer shells of the cylindrical array are accelerating the heavier inner shells (heavier only in that we are assuming a few outer shells accelerate the majority of the plasma material interior to them toward the z-axis). These types of instabilities are characteristic of certain cosmic phenomena also, such as supernova remnants.

where n is the particle density.

To see why this is the case, I have outlined below a derivation of the ionization parameter given by Liedahl in his lecture on the x-ray spectral properties of photoionized plasmas and transient plasmas at the Astrophysics School X (8). We begin by writing an equation of ionization equilibrium, with the ionization processes on one side and the recombination processes on the other. Given a photoionization rate β_i (s^{-1}), a collisional ionization rate C_i (cm^3 s^{-1}), and the recombination rate α_{i+1} (cm^3 s^{-1}) which includes both dielectronic and radiative recombination, the ionization equilibrium equation is of the form

$$n_e C_i n_i + \beta_i n_i = n_e \alpha_{i+1} n_{i+1}, \qquad (1.4)$$

where n_e is the electron density, n_i is the density of ions with charge state i, and n_{i+1} is the density of ions with charge state $i+1$. Note that this equation is identical to Eq. 1.1, except for the "new" term, $\beta_i n_i$, which takes into account the photoionization processes.

We choose to subsitute for the photoionization rate β which depends on the radiation energy density. At a radius r from the radiation source and for a photon energy of ϵ the energy density $U_\epsilon(\epsilon)$ (erg cm^{-3}) is given by

$$U_\epsilon(\epsilon) = \frac{f_\epsilon(\epsilon)}{c} = \frac{L_\epsilon(\epsilon)}{4\pi r^2 c}, \qquad (1.5)$$

where $L_\epsilon(\epsilon)$ is the energy specific luminosity and c is the speed of light. Since the power of the x-ray source for any given photon energy interval is simply a fraction of the total power of the source, we can specify an energy-dependent spectral function which when multiplied to the total luminosity gives the luminosity for a specific energy. Obviously, we should require this spectral function be normalized, such that the fractions for all energies sum together to 1: $\int_{-\infty}^{\infty} f_\epsilon(\epsilon)\, d\epsilon = 1$. Using this normalized spectral function, the energy specific luminosity is given by $L_\epsilon(\epsilon) = L f_\epsilon(\epsilon)$ (both have units of erg s^{-1} since $f_\epsilon(\epsilon)$ is unitless), so we can rewrite Eq. 1.5 as

$$U_\epsilon(\epsilon) = \frac{L f_\epsilon(\epsilon)}{4\pi r^2 c}. \qquad (1.6)$$

If we refer to the energy dependent photoionization cross section of charge state i as $\sigma_i(\epsilon)$ (cm^2) and the photoionization threshold energy (i.e. the minimum photon energy required to ionize an electron of an ion in charge state i) as χ_i, then the photoionization rate β_i will be given by

$$\beta_i = \int_{\chi_i}^{\infty} \frac{c}{\epsilon} U_\epsilon(\epsilon) \sigma_i(\epsilon)\, d\epsilon, \qquad (1.7)$$

where we are integrating the photoionization rate over all photon energies greater than the threshold energy of photoionization from start state i to charge state $i+1$. We can simplify

this expression as

$$\beta_i = \frac{L}{r^2} \Phi_i, \tag{1.8}$$

where $\Phi_i = \frac{1}{4\pi} \int_{\chi_i}^{\infty} \frac{\sigma_i(\epsilon)}{\epsilon} f_\epsilon(\epsilon) \, d\epsilon$. If we substitute this expression for the photoionization rate into Eq. 1.4 and then divide by the electron density, we are left with

$$(C_i + \xi \Phi_i) \, n_i = \alpha_{i+1} n_{i+1}, \tag{1.9}$$

where we have set the ionization parameter to be

$$\xi = \frac{L}{n_e r^2}, \tag{1.10}$$

as defined in Eq. 1.3. Now, we can rearrange Eq. 1.9 to

$$\frac{n_{i+1}}{n_i} = \frac{C_i}{\alpha_{i+1}} \left(1 + \frac{\xi \Phi_i}{C_i} \right), \tag{1.11}$$

where $\frac{C_i}{\alpha_{i+1}}$ is equivalent to the collisional ionization equilibrium ratio $\left(\frac{n_{i+1}}{n_i} \right)_{CIE}$. Thus, the term $\frac{\xi \Phi_i}{C_i}$ is a measure of the degree of overionization. Now, as mentioned earlier, if we fix the temperature of the ionizing source (and thus Φ_i) and choose an electron temperature (thereby choosing a value for C_i and α_i), the degree of relative importance of photoionization processes and collisional processes is fully determined by the ionization parameter. For a larger ionization parameter, photoionization processes are dominant, and for a smaller ionization parameter, collisional processes are dominant. Thus, for a fixed luminosity for the ionizing source, the gas have a higher degree of photoionization for smaller values of r and n_e.

For the gas cell experiment, we can use Eq. 1.3 to calculate the ionization parameter at the center of the gas cell at a specific time in the experiment (or simulation). Note that several of the numerical values quoted below come directly from the simulations described in chapter 2. At $t = 100$ ns, the luminosity or power of the pinch is 1.682×10^{21} erg sec^{-1} and the radius is 0.055 cm. Also at that time, at a position near the center of the gas cell, $r_{cell} = 0.578$ cm, the mass density is 3.6×10^{-5} g cm^{-3}. Since the cell is filled with neon gas, we can compute the particle density by dividing the mass density by the the atomic weight of neon and multiplying by the mean number of ionized electrons in the medium. The atomic weight of neon is 20.180 atomic mass units or 3.35×10^{-23} grams, which implies that the ion density is 1.075×10^{18} cm^{-3}. If we approximate the average number of free electrons for every neon ion to be 8.5, then the particle density is approximately 9.138×10^{18} cm^{-3}. We also must compute the radial distance from the pinch to the piece of the gas cell in question, which is simply the sum of the radial distance from the pinch to the face of the gas cell and

the gas cell radius. This sum amounts to 6.228 cm, which when combined with the pinch luminosity and particle density, yields an ionization parameter of ~ 5 erg cm s^{-1}. From Fig. 1.8 we can see that for a cosmic x-ray photoionized nebula the ionization parameter is of order several hundred erg cm s^{-1}. Note that in the figure the contours are of $\log(\xi)$, not ξ.

Given the current setup of the gas cell experiments, the gas plasma created in the cell is photoionized to a degree several magnitudes less than that of cosmic x-ray photoionized nebulae. Future experiments could increase the value of the ionization parameter for the laboratory plasma by lowering the density (at the expense of absorption and emission line strength), moving the cell closer to the pinch (at the risk of increasing both the temperature gradient across the cell and bulk hydrodynamic motion within the cell), or increasing the luminosity of the Z-pinch (either by increasing the current flow or by implementing different wire array configurations).
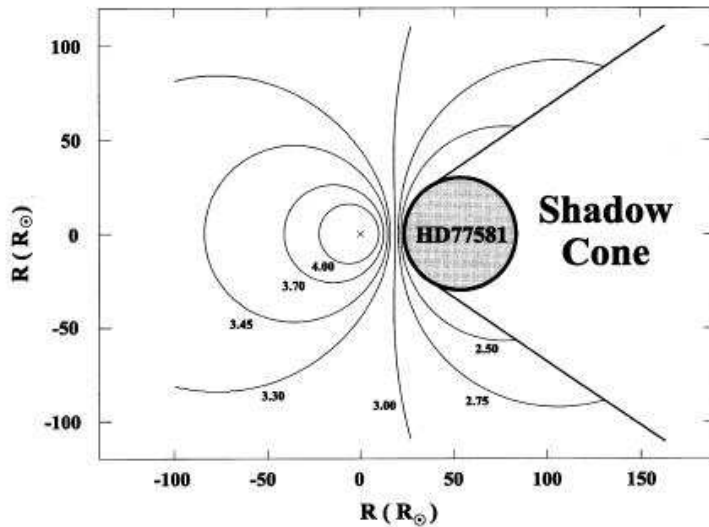

Fig. 1.8.— Contours of constant ionization parameter (logarithmic) plotted for the region surrounding the HMXRB Vela X-1. Figure taken from (16).

1.7.   Scope of the thesis

The scope of my thesis is three-fold. First, simulation codes are used to model a gas-cell experiment (shot Z543) that was conducted on the Z machine at Sandia National Laboratories by Jim Bailey (1). The absorption spectrum synthesized using the simulation codes is compared to the absorption spectrum measured in the actual experiment. By identifying differences between the synthesized and measured spectra, we are able to calibrate our

modeling procedure so that we can more accurately model the experiment.

Once the modeling procedure has been validated using experimental data, we are able to enter the second stage of the research: use the same modeling procedure to design new gas cell experiments. Essentially, this equates to testing the effect of changing different experimental parameters, such as gas cell fills, geometries, and positions. If modifying one of these experimental parameters yields an interesting result in the spectrum, then modifying that parameter in the actual experiment may prove to be useful and insightful.

The third and last stage of the research involves using the modeling procedure to synthesize new diagnostics of the photoionized plasma; namely, time dependent absorption and emission spectra. Our goal is to eventually measure these time dependent spectra in the experiment, so it will be important to have synthesized spectra to which we can compare when we conduct the actual observations.

2.   Modeling

Our modeling procedure is a multi-stage simulation process which at each stage uses the results of the previous stage(s) to compute another result. Because each successive simulation is dependent on the simulation(s) that preceded it, this modeling process has a well defined chronological procedure. This procedure is outlined in a flow chart in Fig. 2.1.

There are three main stages of the modeling procedure: [1] compute the incident flux on the face of the gas cell; [2] compute the position and time-depedent temperature and density distributions of the gas in the cell; and [3] synthesize an emission or absorption spectrum. For step [1] we use a 3-D viewfactor code to represent the experimental setup and calculate the radiation field. The values of the albedos for the surfaces are intially assumed and then constrained by modeling, and the time-dependent pinch radius and power are taken from experimental measurements as described in Section 2.1. The final result of this step is a time-dependent incident spectrum for a representative surface element of the face of the gas cell. Step [2] inputs the incident flux result of step [1] in addition to EOS and opacity models for all of the gas cell materials, and then performs a non-LTE radiation-hydrodynamics simulation that computes the time-dependent temperature and density distributions of the gas in the cell. This result is used along with the incident spectrum from [1] and detailed atomic level and transition data to synthesize an absorption or emission spectrum in step [3].

The codes implemented for these simulations are [1] *VisRad* (14), a 3-D viewfactor code, [2] *Helios* (11), a 1-D Lagrangian hydrodynamics code, and [3] *Spect3D* (13), a spectral synthesizer. Also employed for these simulations are *AtomicModelBuilder* (10), a program used to create custom atomic models from the ATBASE atomic database, and *Propaceos* (PRism OPACity and Equation Of State) (12), a program that generates equation of state (EOS) and multigroup opacity models. Information on all of these referenced codes is available online at `http://www.prism-cs.com/Software/Software_overview.htm`.

2.1.   VisRad

The first component in our modeling procedure involves calculating the incident flux at the face of the gas cell. For this task we employ the viewfactor code *VisRad* (5). While the gas cell experiments are similar to the x-ray binary system in that the pinch generates a large x-ray flux which can photoionize nearby cool gas, the laboratory experiments differ from the cosmic system in that there are numerous surfaces that can absorb and reemit the radiation emitted by the pinch or reflected by other surfaces. Certainly, in an astrophysical environment, one might approximate the incident flux at a remote location using the inverse
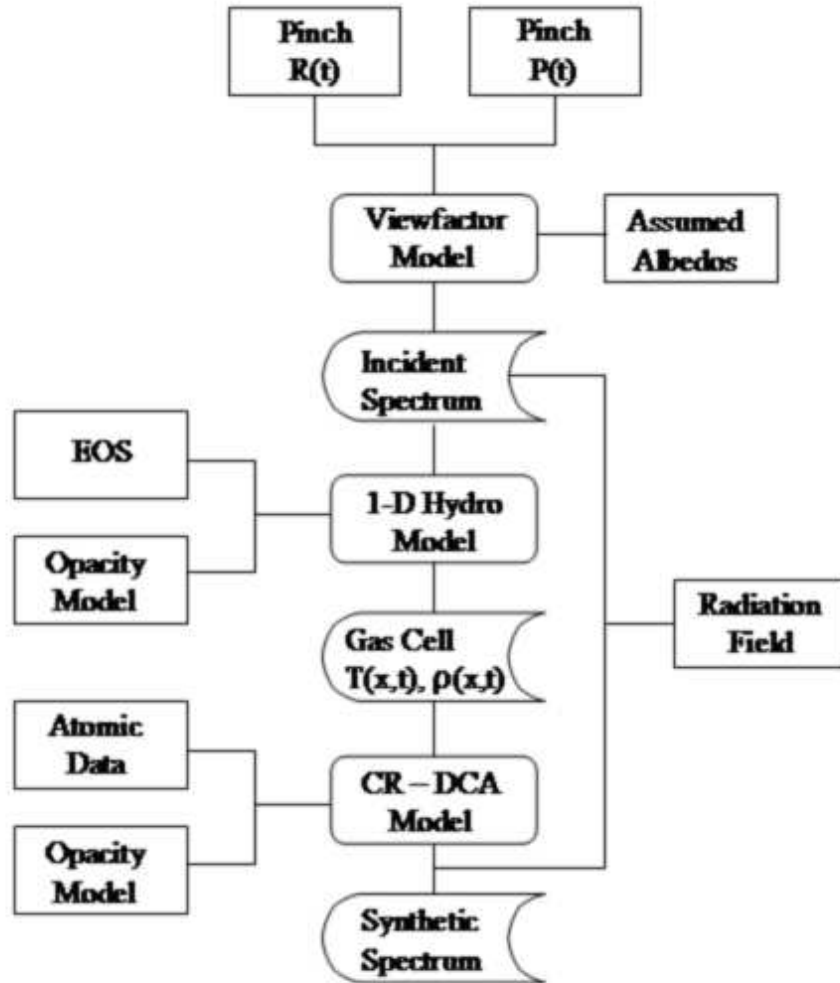
Fig. 2.1.— Flow chart of modeling procedure. Recall that the time-dependent pinch radial and power data are measured in the actual experiment, and that the albedos are only assumed initially - several iterations of the viewfactor simulation allow us to constrain their values.

square law given by Eq. 1.2. In the gas cell experiments, however, this approximation is not a good one to make since, as already mentioned, there are many metal surfaces which absorb and reemit radiation. Additionally, the pinch is not approximated well by a point source emitting isotropically (which the inverse square law assumes of the source) because it is extended within the field of view of the gas cell and is not spherically symmetric. *VisRad* allows us to model all of these metal surfaces, and then calculate the contribution of these surfaces to the incident flux at the face of the gas cell. See Fig. 2.2 for a plot of the incident spectra on the center of the gas cell from the different surfaces in the experiment. Notice that the contributions from the surfaces other than the pinch are non-neglible for lower photon energies, which is precisely why it is necessary to use a viewfactor code to calculate the incident spectrum on the gas cell.
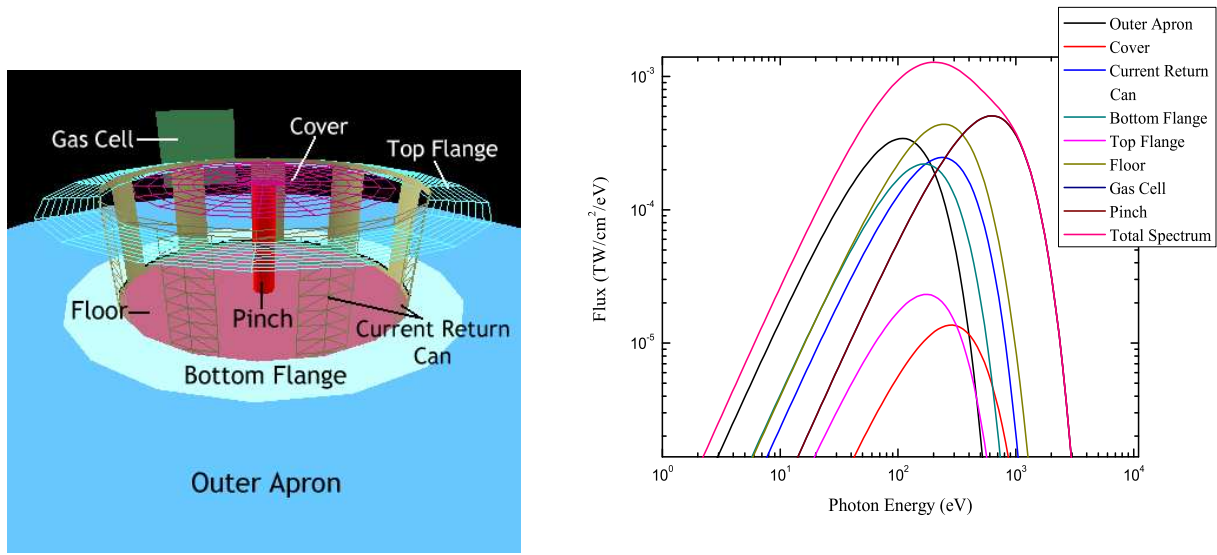

Fig. 2.2.— To the left is a screenshot of the *VisRad* workspace with the different surfaces labeled, and to the right is a plot of the contributions to the incident spectrum on the center of the gas cell at $t = 100$ ns, the peak of x-ray emission from the pinch. Notice that the pinch contributes the bulk of the high energy incident flux, but also that the contributions of the other surfaces, especially for lower energies, are not negligible.

2.1.1. Constructing a Workspace

Before the incident spectrum on the gas cell can be calculated, however, the experimental setup must first be constructed in the *VisRad* simulation workspace. Similar to how an

experimentalist might set up the experiment on the actual Z-machine, the experimental setup is modeled piece by piece by constructing wire-frame structures and applying surface elements to them. For example, the face of the gas cell is modeled as a square wire frame, with 25 surface elements. In other words, the front surface of the cell is represented by a 5×5 element grid. As will be shown in Section 2.1.3, the surface elements are key to computing the incident radiation on the gas cell, since each *viewfactor* is a function between two surface elements. As a result, the number of total surface elements is directly related to the degree of accuracy of the viewfactor simulation. The tradeoff, of course, is that the number of viewfactors increases rapidly as more surface elements are used, thereby causing the computation time to increase as the number of surface elements increases.

The objects are positioned and oriented in a 3-D spatial grid in the same positions and orientations they have in the actual experiment. Material properties that govern the object's rate of absorption and emission – like albedo (how *reflective* the object is), emitted power, and laser reflectivity and x-ray conversion efficieny (not important for modeling the gas cell experiments, but a crucial parameter for modeling inertial confinement fusion (ICF) experiments) – can also be specified for the surfaces in the *VisRad* workspace. See Fig. 2.3 for screenshots of the underlying wireframe structure of the workspace objects and the metal surfaces colored by emission temperature for a simulation time just before the peak of the pinch emission and Table 2 for a list of the positions, orientations, dimensions, and material properties of all objects in the *VisRad* model of the gas cell experiment.

2.1.2. Input Parameters

VisRad supports multiple time-step simulations in which dimensions or material properties of objects in the workspace can change with time. The time-dependence of these object parameters can be specified by inputting a table of time-dependent values. It is important to recognize (important enough that this issue will be revisited again in Section 2.1.3) that while adding time-dependence to the parameters in the experiment forces the simulation results to be time-dependent, the simulation result for any single time-step is independent of the flux distribution at any other time-step. This approximation is certainly valid for times before the peak pinch emission, since all of the surfaces are relatively cold and have negligible self-emission. After the peak of the pinch emission, however, the surfaces should be hotter and therefore have a larger degree of self-emission. Though, because the pinch emission is still so much larger than the emission of these surfaces for times after the peak of the pinch emission, it seems reasonable to approximate the total emission from the surfaces using only the surface albedo and the incident flux (due to the pinch and other surfaces absorbing and reemitting the pinch emission).
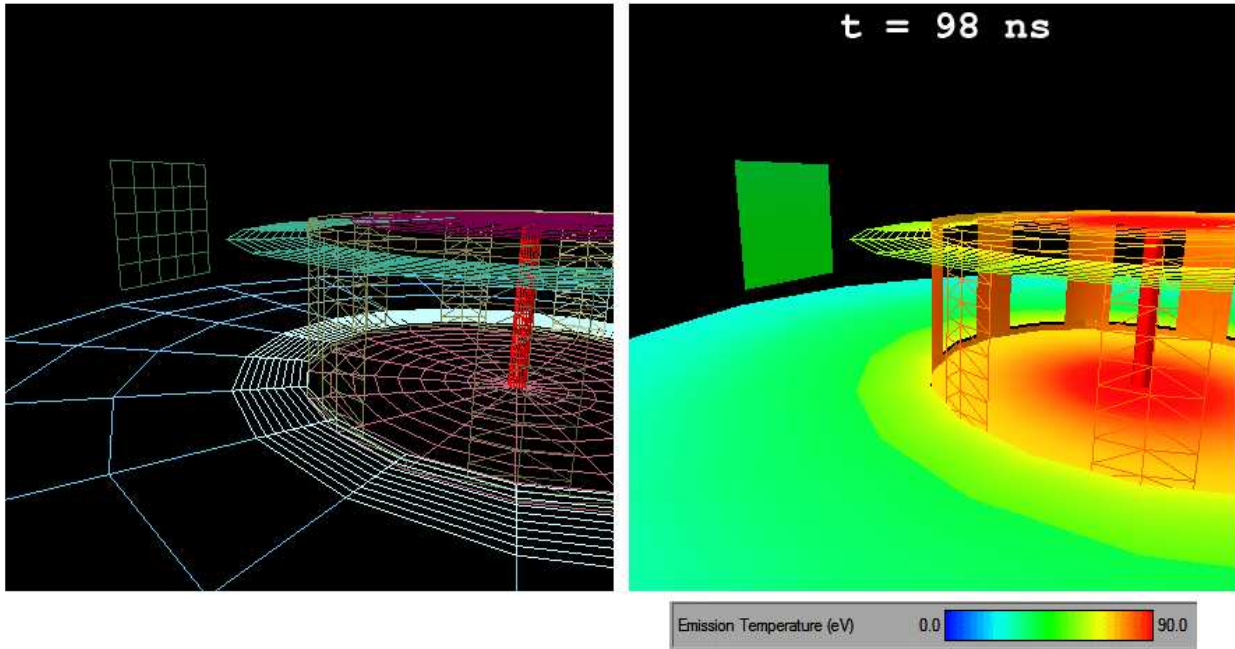
Fig. 2.3.— To the left is a screenshot of the wireframe grid modeling the setup for the gas cell experiment. To the right is a screenshot from the viewfactor simulation, showing emission temperature of the surfaces at a time right before the peak emission of the pinch.

In the gas cell experiment, the radius of the pinch decreases as the experiment progresses, so we inputted a time dependent table of values for the radius of the pinch. These time-dependent radial values are plotted in Fig. 2.4.

As mentioned earlier, *VisRad* gives the user the option to specify values for the material properties of the object; namely, the albedo and power. Just as we could for the dimensions of the object, we can also make any one of these material properties time dependent by importing a table of times and corresponding property values. For the Z-pinch, the power increases as the radius decreases up until a peak time, and then decreases after the peak. This behavior is shown in Fig. 2.5.

It is important to note that the time-dependent pinch radius and power are not inferred from other quantities or the result of any modeling simulation; rather, these time-dependent pinch data are directly measured in the actual experiment. The radius is measured using a combination of a framing x-ray pinhole camera (FPC) and the Energy-Space-Time (EST) 1-D streaked imager. The power is measured using a filtered x-ray diode array (XRD) in conjunction with a bolometer (15). The other important parameter in modeling the experiment, i.e. the surface albedos, are not measured directly in the experiment and are instead constrained using an iterative process described by Rochau in his PhD thesis (15).
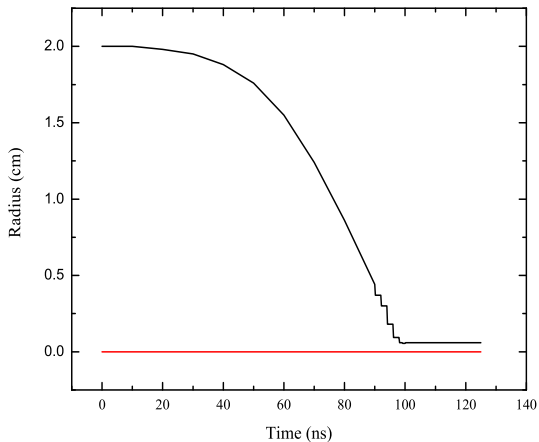
Fig. 2.4.— Time-dependent radius of the pinch. The red line is simply an asymptote at $y = 0$. The jagged feature preceding 100 ns is the result of the interpolation of data points.
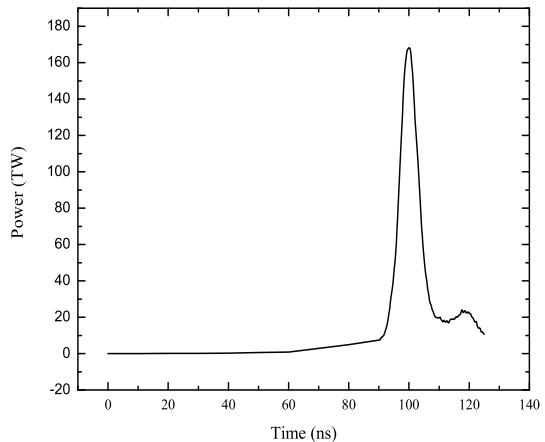
Fig. 2.5.— Time-dependent power of the pinch. Notice that the power of the pinch peaks at approximately 100 ns, and then decreases at a similar rate to its increase before the peak.

The process begins by assuming values for the albedos and then, using the calculated incident flux on each surface and a 1-D radiation-hydrodynamics simulation, calculates the plasma reemission from each surface (i.e. a new albedo). This process is repeated until the power of the surface converges at each time-step. The final time-dependent values of the surface albedos for several objects in the experimental setup are shown in Fig. 2.6.

Using the time-dependent radial and power data, one can calculate the time-dependent emission temperature of the pinch. In general, we can relate the flux through a unit area on a surface to the luminosity by the equation

$$f = L/A, \tag{2.1}$$

where f is the surface flux, L is the luminosity, and A is the surface area of the radiating object. Now, if we approximate the pinch as a blackbody, we can apply the Stefan-Boltzmann law, which states that the total energy radiated per unit time (i.e. the power) per unit surface area (i.e. the flux) is directly proportional to the fourth power of its temperature, which we will call its emission temperature. Thus,

$$f = \sigma T_{em}^4, \tag{2.2}$$

where the proportionality constant σ is the Stefan-Boltzmann constant. Solving for the flux
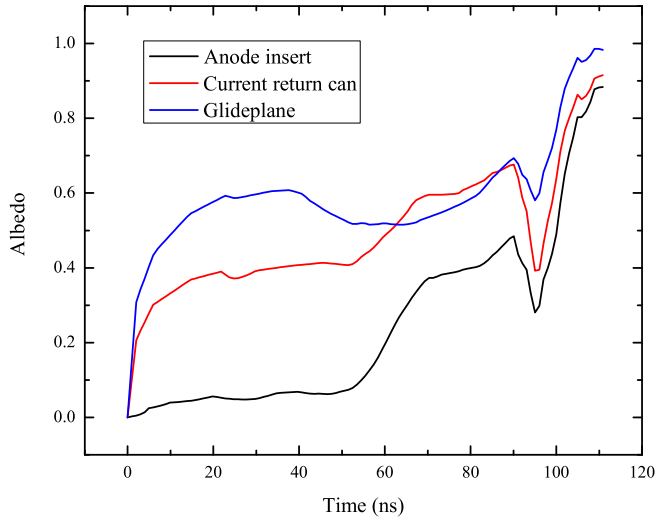
Fig. 2.6.— Time-dependent values of the albedo for three "classes" of surfaces in the experiment. The label *anode insert* refers to what has been previously called the *outer apron*, the label *glideplane* to the *cover* and *floor*, and the albedo model for the *current return can* also applies to the *bottom* and *top flanges*. For a diagram of the experimental setup with these surfaces labeled, see Figure 2.2. Albedo model taken from (15).

in either equation, we obtain

$$T_{em} = \left[\frac{L}{A\sigma}\right]^{\frac{1}{4}}. \tag{2.3}$$

Fig. 2.7 is a plot of the time-dependent pinch emission temperature.

An interesting feature of the emission temperature plot is the assymmetry about the peak of the emission. On the power plot, the data is very symmetric about the peak at $t = 100$ ns, but on the emission temperature plot there is a shoulder to the right of the peak. At first, one might think that the emission temperature curve behavior should mimic that of the power curve, but Eq. 2.3 tells us that for a constant power (i.e. times symmetric about the power peak)

$$T_{em} \propto A^{-\frac{1}{4}} \propto R^{-\frac{1}{4}} \tag{2.4}$$

since if we approximate the pinch as a cylinder, $A = 2\pi Rh$, where R is the radius and h is the height. Thus, if we consider two times symmetric about the pinch power peak, $t = 96$ ns and $t = 104$ ns for example, the power of the pinch at both of those times will be nearly constant, so the emission temperature will depend solely on the radius of the pinch. Since at a later
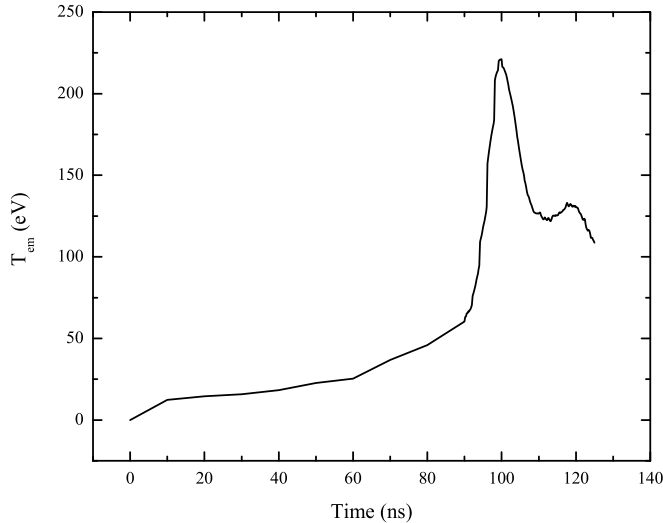
Fig. 2.7.— Time-dependent emission temperature of the pinch calculated using Eq. 2.3 and the pinch radial and power data shown in Fig. 2.4 and 2.5 respectively.

time the pinch radius will be smaller, the emission temperature of the pinch will be higher at that time. This is precisely why there is a shoulder in the pinch emission temperatures for later times, and is also why the emitted flux of the pinch following the peak at $t = 100$ ns is greater than the emitted flux preceding the peak (since according to Eq. 2.2 the flux is proportional to the fourth power of the emission temperature).

The reason why we are interested in the functional form of the pinch emission temperature as a function of time is that this temperature profile, and not the power profile, sets the radiative emission profile of the pinch. As will be discussed in Section 2.1.3, the surface elements of the pinch are approximated as blackbodies with an emission spectrum set by their emission temperature T_{em}. Thus, knowing the emission temperature of the pinch is equivalent to knowing the emission spectrum of the pinch.

2.1.3.   How does the code work?

As described by MacFarlane (5), the 3-D viewfactor code *VisRad* computes the radiative flux incident on a single surface i element by solving the radiosity equation given by

$$B_i - \alpha_i \sum_j F_{ij} B_j = Q_i, \qquad (2.5)$$

where B_i is the emitted flux from surface i (erg s^{-1} cm^{-2}), α_i is the surface albedo, Q_i is the source term, and F_{ij} is the viewfactor between surface i and surface j. The first term on the left, B_i, is the amount of flux emitted by the surface i itself. Note that for the gas cell experiments the pinch is the primary x-ray source, so the surface of the pinch is the only surface in the experiment with nonzero Q_i source terms, and these source terms are set by the emission temperature profile of Fig. 2.7. Using the Stefan-Boltzmann equation (Eq. 2.2), we can convert this flux into an emission temperature, given by

$$T_{em,i} = \left[\frac{B_i}{\sigma} \right]^{\frac{1}{4}}. \tag{2.6}$$

The second term on the left of Eq. 2.5 is the amount of radiated flux from all other surface incident upon surface i that is reflected from surface i. The limits of the albedo coefficient α_i are 1, for a fully reflective surface, and 0, for a fully absorbant surface. The summation adds up the contributions from all other surfaces j by computing for each surface j the viewfactor between surface i and j (the fraction of energy leaving surface j and arriving at surface i, see Section 2.1.4) and then multiplying that by the emitted flux of j. Thus, this summation computes the total radiative flux from all other surfaces j incident upon surface i:

$$q_i^{in} = \sum_j F_{ij} B_j, \tag{2.7}$$

where q_i^{in} is the incident flux (erg s^{-1} cm^{-2}). Once again, we can apply Eq. 2.2, and convert this flux to a radiation temperature, given by

$$T_{rad,i} = \left[\frac{q_i^{in}}{\sigma} \right]^{\frac{1}{4}}. \tag{2.8}$$

We are further interested in how the incident flux varies with frequency (i.e. what the incident spectrum on surface i looks like), since the surfaces in the experiment will emit at a wide range of frequencies. Assuming each surface element to emit like a blackbody, the spectrum of each element will be given by the Planck function $B_\nu(T_{em,j})$, where $T_{em,j}$ is the emission temperature of surface j. Now, it can be shown that the Planck function integrated over all frequencies gives

$$\int_0^\infty B_\nu(T_{em,j}) \, d\nu = \frac{\sigma T_{em,j}^4}{\pi}, \tag{2.9}$$

which implies that the emitted flux at a single frequency is given by

$$B_j(\nu) = \pi B_\nu(T_{em,j}). \tag{2.10}$$

Substituting this new expression for the radiated flux from surface j in Eq. 2.7, our final expression for the frequency-dependent incident flux on surface i is

$$q_i^{in}(\nu) = \sum_j F_{ij} \pi B_\nu(T_{em,j}).$$

(2.11)

Computing the incident flux for each frequency produces an incident spectrum for surface i. Often, we choose the surface element at the center of the gas cell as representative of the entire face of the gas cell, and output the spectrum incident on that surface. The result is shown in Fig. 2.8.

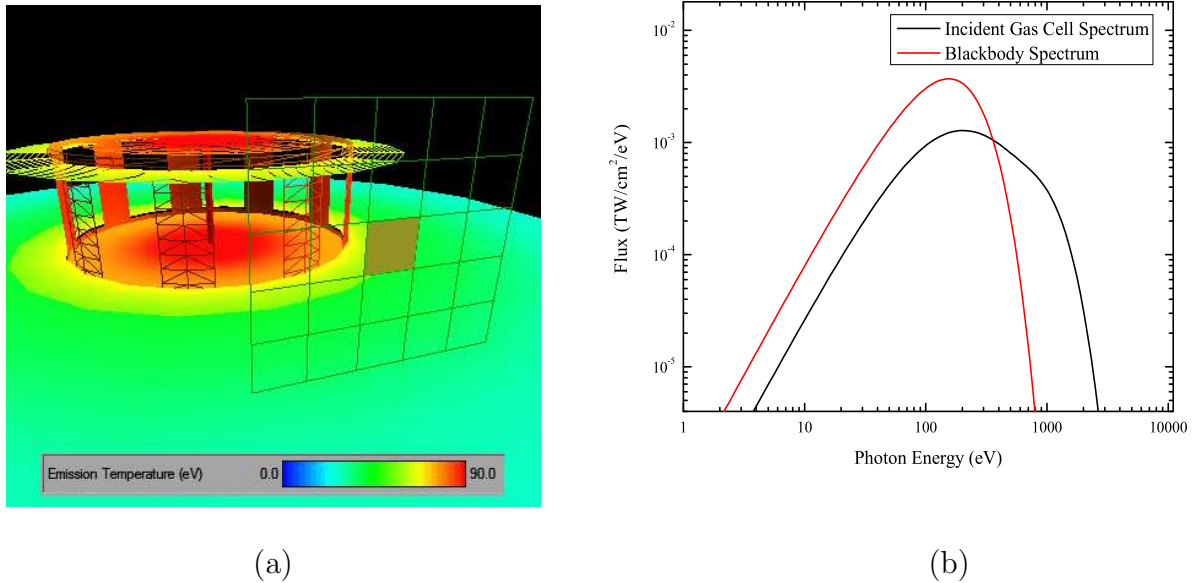(a)   (b)

Fig. 2.8.— (a) *VisRad* screenshot of workspace after the simulation has completed. The highlighted portion of the gas cell is the representative surface element we use to measure the incident spectrum on the gas cell. (b) The spectrum incident upon the highlighted surface element at $t = 100$ ns and an *equivalent* blackbody of temperature equal to the radiation temperature of the highlighted surface element. Note the distinctly non-Planckian shape of the calculated incident gas cell spectrum.

For each time step in the simulation, *VisRad* recomputes the radiosity balance using Eq. 2.5. This means that the code calculates an emission and radition temperature for every surface element at each time step. To be clear, though, the emission and radiation temperatures calculated at each step are not dependent upon any other time step in the

simulation. That is, at each time step, the flux distribution is determined from a coupled set of *steady-state* power balance equations, and this distribution is independent of the distribution at any other time.

2.1.4. Calculation of Viewfactors

As mentioned in section 2.1.3, the viewfactor between surface i and j is physically the fraction of energy leaving surface i and arriving at surface j. At each time-step of the simulation, *VisRad* recomputes the mutual viewfactor between each surface, so in understanding how *VisRad* computes the incident flux on the face of the gas cell it is crucial that we understand how these viewfactors are calculated. To begin, let us first consider a plane surface, dA_i, which is emitting an intensity of radiation along the surface normal given by I_0 (erg s^{-1} cm^{-2} sr^{-1}). The intensity is related to the flux in the following way (for a blackbody emitter):

$$F(T) = \sigma T^4 = \pi I(T). \tag{2.12}$$

Thus, we can write, using Lambert's Cosine Law (see Fig. 2.10(a)):

$$I_{\theta_i} = I_0 \cos \theta_i = \frac{\sigma T^4}{\pi} \cos \theta_i. \tag{2.13}$$

The angular size of the solid angle through which this intensity is emitted at an angle θ_i is given by

$$d\Omega_{\theta_i} = \sin \theta_i d\theta d\phi, \tag{2.14}$$

so the intensity of radiation through the differential solid angle at an angle of θ_i is

$$I_{\theta_i} d\Omega_{\theta_i} = \frac{\sigma T^4}{\pi} \cos \theta_i \sin \theta_i d\theta d\phi. \tag{2.15}$$

The fraction of this intensity that will hit surface dA_j is the ratio of the area of dA_j projected into the plane of the solid angle divided by the area of the solid angle at a distance R_{ij}. The area of dA_j projected into the plane of the solid angle is simply $dA_j \cos \theta_j$ (recall Lambert's Cosine Law), so the ratio of this area to the area of the solid angle at R_{ij} is

$$ratio = \frac{dA_j \cos \theta_j}{R_{ij}^2 \sin \theta_i d\theta d\phi}. \tag{2.16}$$

The product of this ratio of areas and the intensity of radiation (through the solid angle $d\Omega_{\theta_i}$) is the total intensity incident upon surface dA_j from surface dA_i.

$$dI_{ij} = \frac{\sigma T^4 \cos \theta_i \cos \theta_j dA_i dA_j}{\pi R_{ij}^2}. \tag{2.17}$$

Since σT^4 is proportional to the energy emitted by dA_i, then the differential *viewfactor* between surface da_i and surface dA_j is

$$dF_{ij} = \frac{\cos\theta_i \cos\theta_j dA_i dA_j}{\pi R_{ij}^2}.$$ (2.18)

VisRad computes the viewfactor between each surface in the workspace by integrating the differential viewfactors over all surface elements of each surface. The result of this integration, F_{ij} is used to calculate the incident flux on each surface element in the workspace.

2.1.5. Spatial variation of incident flux on the face of the gas cell

Since the calculated incident flux on only one surface element of the gas cell is taken as representative of the incident flux hitting the entire face of the gas cell, it is important to investigate the spatial variation of the flux incident on each surface element of the face of the gas cell to ensure this approximation is not an unreasonable one to make. If we take all surface elements of the face of the gas cell to be relatively equidistant from the pinch, then the fraction of the pinch the surface element *sees* will dictate how much flux is incident upon that surface element. Whether a given surface element sees none, a fraction, or the entire pinch is dependent on two factors: [1] the vertical and azimuthal position of the gas cell, and [2] the slot geometry of the current return can. The current return can is a gold cylindrical enclosure surrounding the pinch through which the *positive* current *returns* to the outer apron after passing through the pinch. In order to allow radiation from the pinch to propagate to the gas cell, holes or *slots* are cut into the current return can. If the position of the gas cell is held constant, then the geometry of these slots (their size and location) completely determines how much of the pinch each gas cell surface element can see. Similarly, once the geometry of the slots in the current return can has been established, then the position of the gas cell becomes critical to determining how much of the pinch different parts of the gas cell can see. If the gas cell is placed too high, the upper portions of the gas cell will have a reduced or no view of the pinch because of obscuration by the top flange and cover. If the gas cell is centered on an azimuthal angle that places it directly behind one of the current return can walls, then only the outer edges of the gas cell will have an unobscured view of the pinch. Shown in Fig. 2.11 are the views of the pinch from several different locations on the gas cell. Notice that the surface elements labeled "CENTER" and "SIDE" see the entirety of the pinch, while the surface element labeled "TOP" sees only a fraction of the pinch because part of its view is blocked by the top flange and cover.[4] The

---

[4]As you may have noticed, in the *VisRad* screenshot from the "TOP" position the top portions of the pinch are actually visible through the cover and top flange. This is a feature of the *VisRad* program known

partially obscured view of the pinch from the upper surface element of the gas cell is the reason why in Figure 2.9 there is a vertical temperature gradient on the face of the gas cell for peak times in the pinch emission. This gradient is also shown quantitatively in Figure 2.12.

Also included in Fig. 2.12 is a plot of the incident spectrum on each of the three representative surface elements at $t = 100$ ns in the viewfactor simulation. Not suprisingly, the flux incident on the "SIDE" and "CENTER" surface elements is nearly the same, whereas the flux on "TOP" surface element is lacking the high energy shoulder that the other two spectra have. As was shown in Fig. 2.2 the pinch is the major contributor of the high energy flux at $t = 100$ ns, so it makes sense that the surface element that sees only a fraction of the pinch would receive only a fraction of the high energy flux from the pinch. Of course, as mentioned earlier, the other surfaces also contribute to the flux incident on the gas cell, but the point to be made here is that the pinch is the sole contributor of photons of higher energy (namely, those energies greater than ~ 1.5 keV).

This study of the spatial variation of the incident flux on the face of the gas cell demonstrates that given our current placement of the gas cell, a vertical temperature gradient appears at the peak of the pinch emission due to the partial obscuration of the view of the pinch from the upper portions of the gas cell. It is unclear how pronounced an effect this temperature gradient might have on the emission and absorption spectra we measure, but is certainly something to keep in mind if discrepancies between the synthesized and experimental spectra appear.

---

as *scaffolding* which forces surfaces to be displayed as wire frames if they are obstructing the view of objects behind them along the line of sight of the viewer. While this feature is useful for viewing the workspace in its entirety, for the purposes of the viewfactor simulation all surfaces are solid and have no property of transparency.
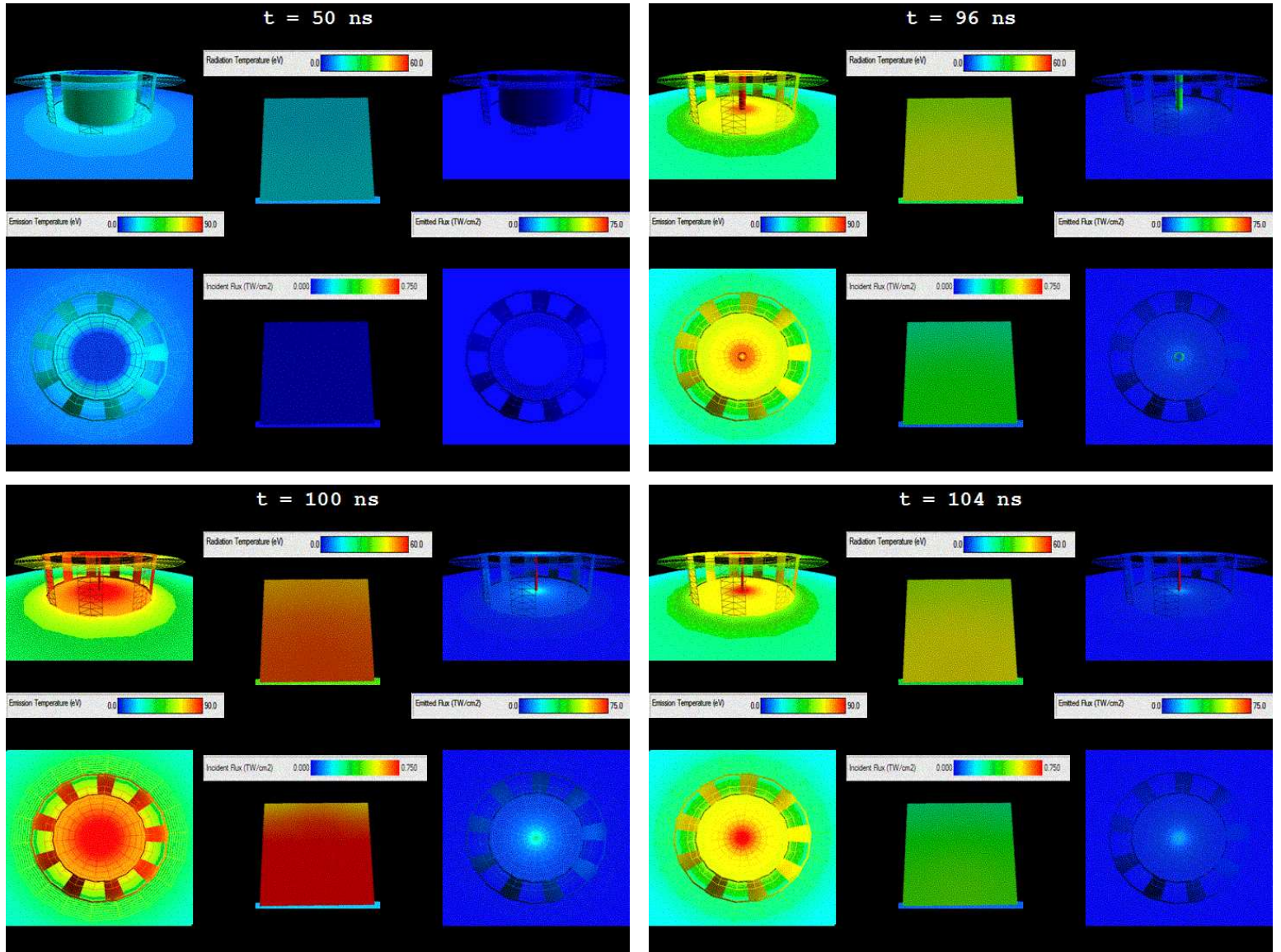
Fig. 2.9.— Compiled snapshots of the *VisRad* simulation for different times. In each snapshot, the gas cell is pictured in the middle column, and the pinch and diode assembly are pictured in the left and right columns.

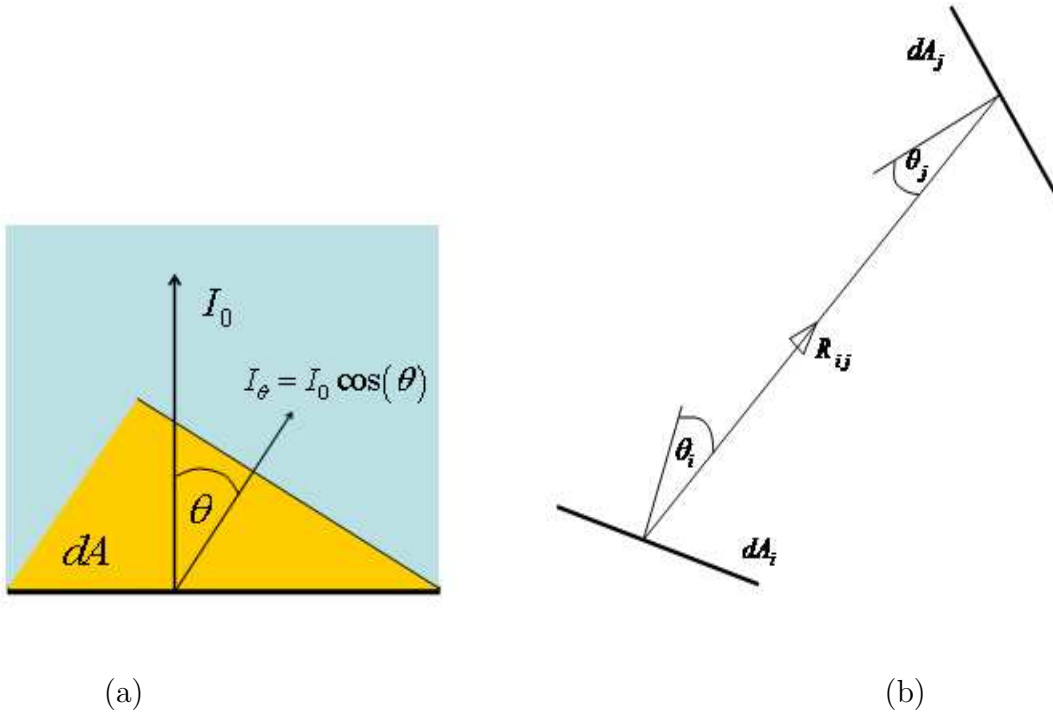(a)   (b)

Fig. 2.10.— (a) Diagram of Lambert's Cosine Law. This law simply says that the amount of radiation an observer receives is proportional to the ratio of the amount of surface area the observer can see to the total surface area. (b) Diagram showing the parameters necessary for computing the viewfactor between two surfaces elements.
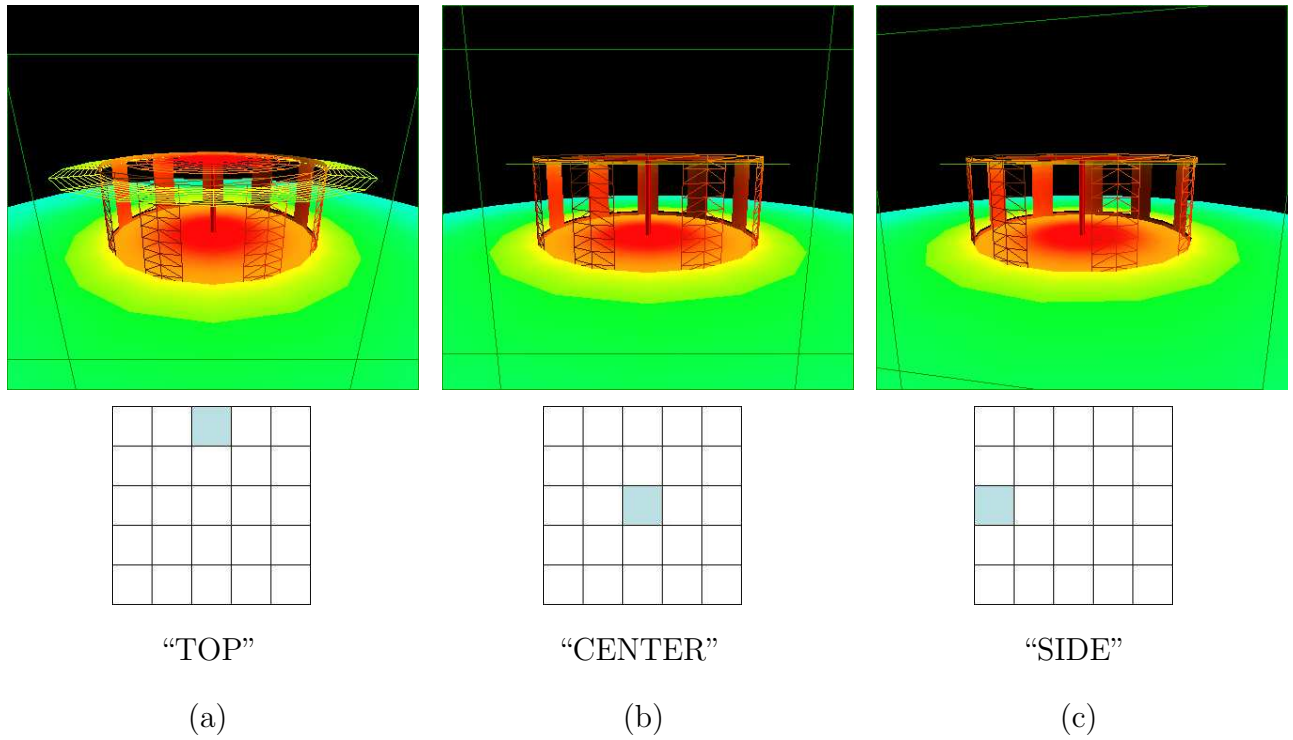
"TOP"

"CENTER"

"SIDE"

(a)

(b)

(c)

Fig. 2.11.— Views of the pinch from surface elements located at the (a) TOP, (b) CENTER, and (c) SIDE of the gas cell. In each column, the top image is a screenshot captured from a viewing position directly behind the relevant surface element of the gas cell. The relevant surface element for each column is highlighted in blue in the diagram immediately below the *VisRad* screenshot.
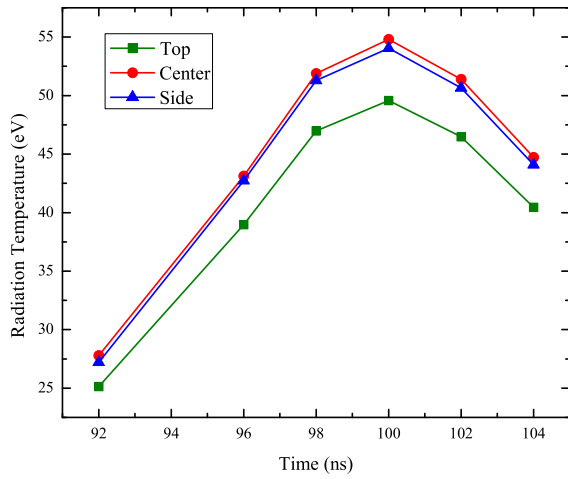
(a)
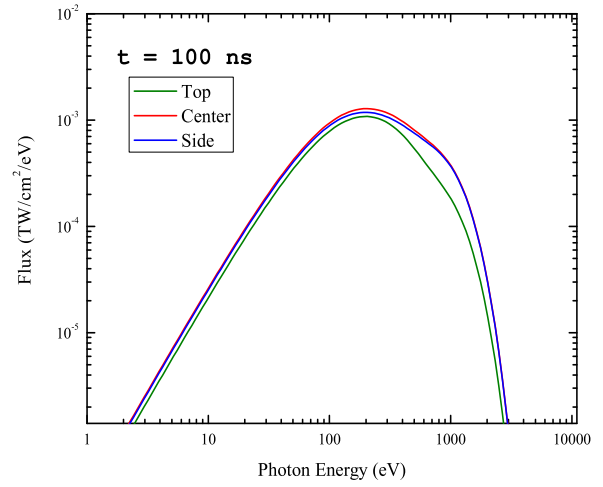
(b)

Fig. 2.12.— (a) Time-dependent radiation temperature of three representative surface elements of the face of the gas cell, and (b) the incident spectrum on each of these surface elements at $t = 100$ ns.

2.2. Helios

In the gas cell experiments, a sample of gas initially at a low temperature and uniform density is bombarded on one side by a large x-ray flux. The rapid non-uniform heating that results from this asymmetric energy flux bombardment gives rise to hydrodynamic motion of the gas in the cell in the form of shock and compressional heating. If we are to synthesize an accurate absorption and/or emission spectrum for the gas in the cell, it becomes vital for these experiments to know how the temperature and density distributions of the gas as in the cell change with time, since these distributions will directly effect how radiation is transferred by the gas. Further, the code used for spectral synthesization, *Spect3D*, does not have the ability to compute a temperature or density for the plasma (via a hydrodynamics simulation or otherwise), so at the minimum this step in the modeling process in necessary in that the spectral synthesizer needs a temperature and density in order to compute an absorption or emission spectrum.

The code employed to calculate the hydrodynamic motions (ultimately calculating time-dependent temperature and density distributions) of the gas in the cell of these experiments is *Helios* (6), a one-dimensional Lagrangian radiation-magnetohydrodynamics code that models the dynamic evolution of high energy plasma. For the purposes of this investigation, the *magneto*hydrodynamic feature of this code is not used, but magnetic fields become much more important when modeling coronal plasmas in objects like the Sun, or even the pinch plasma in the gas cell experiments.

As discussed in detail by MacFarlane et al. in (6), *Helios* solves a series of partial differential equations in order to calculate the time-dependent temperature and density distributions. These equations are derived from conservation considerations, and are as follows:

Mass Conservation

In a Lagrangian hydrodynamic system, the mass of each volume element is conserved because the spatial grid moves with the mass. In this system, the mass of each volume element is given by

$$dm_0 = \rho(r)r^{\delta-1}dr, \tag{2.19}$$

where ρ is the mass density in units of (g cm^{-1}) for a planar geometry, r is the spatial coordinate in units of (cm), and $\delta = 1$ for the planar geometry of the gas cell. The mass conservation criterion can then be expressed explicitly as

$$\frac{\partial V(r)}{\partial t} = \frac{\partial}{\partial m}(r^{\delta-1}u), \tag{2.20}$$

where $V(r)$ is the specific volume, ρ^{-1}, in units of (cm g^{-1}), and u is the fluid velocity in units of (cm s^{-1}). This equation says that the rate of change of the volume per unit mass is

equal to the derivative (with respect to the mass) of the rate at which the mass is moving (since the spatial coordinate goes to 1 for $\delta = 1$). Essentially, this means that the rate of the change of the specific volume (the volume per unit mass) at a certain radius must equal the rate at which mass is leaving (or arriving) at that radius. One might think of this as the specific volume *stretching* to accomodate new mass and *compressing* to compensate for lost mass. As expected, this implies that the the spatial grid *moves* with the mass in this system.

Momentum Conservation

If we approximate the flow of the plasma as a single fluid (electrons and ions flow together at the same rate), then the equation of momentum conservation is

$$\frac{\partial u}{\partial t} = -r^{\delta-1}\frac{\partial}{\partial m_0}(P_e + P_i + P_r + q) \tag{2.21}$$

where P_e, P_i, P_r are the electron, ion, and radiation pressures respectively, and q is known as the Von Neumann artificial viscosity. If we think of pressure as an energy density, having units of (erg cm^{-1}) for a planar geometry, then the derivative with respect to mass has units of force per unit mass, or acceleration (cm s^{-2}), which as expected matches the units of the derivative of the fluid velocity on the left. This equation, therefore, is merely a restatement of Newton's second law, $F = ma$, where the left side of the equation is the acceleration and the right side is the force scaled by the mass (since the pressure for a planar geometry is simply the force scaled by the spatial coordinate).

The Von Neumann artificial viscosity term is included to effectively *smooth* shocks by spreading out a rapid increase in pressure over a small number of zones (rather than having a discontinuous pressure increase over a single zone).

Energy Conservation

The equations of energy conservation, written in terms of temperature diffusion equations (for a single temperature model for the electrons and ions) are given by

$$C_{v,e}\frac{\partial T}{\partial t} = \frac{\partial}{\partial m}\left(r^{\delta-1}\xi_e\frac{\partial T}{\partial r}\right) - \left[\frac{\partial E_e}{\partial V} + P_e\right]\frac{\partial V}{\partial t} + R_{Abs} - R_{Emis} \tag{2.22}$$

and

$$C_{v,i}\frac{\partial T}{\partial t} = \frac{\partial}{\partial m}\left(r^{\delta-1}\xi_i\frac{\partial T}{\partial r}\right) - \left[\frac{\partial E_i}{\partial V} + P_i\right]\frac{\partial V}{\partial t} - q\frac{\partial V}{\partial t} \tag{2.23}$$

where T is the temperature (K), C_v is the specific heat capacity (erg K^{-1} g^{-1}), ξ is the thermal conductivity (erg s^{-1} cm^1 K^{-1}) for a planar geometry, E is the specific internal

energy (erg g^{-1}), R_{Abs} is the radiative heating (erg g^{-1} s^{-1}), and R_{Emis} is the radiative cooling (erg g^{-1} s^{-1}). This equation simply states that specific change in energy rate is the sum of all of the heating and cooling processes.

As part of the hydrodynamics calculation, equation of state (EOS) and opacity data are read into the *Helios* workspace. For the gas cell simulations, we used EOS data from SESAME, the Los Alamos National Laboratory Equation of State Database. The opacity data from the simulations came from several different sources depending on the simulation mode and material in question. One of these sources of opacity data was the plasma equation of state and multi-frequency opacity code *Propaceos*.

2.2.1. Propaceos

Helios has the capability of calculating the frequency-dependent absorption and emission opacities used to calculate the radiation absorption and emission terms in the energy conservation equation for each time-step in the simulation. While this method of determining the opacities from the atomic level populations at each time-step is the most accurate way to model the system, as might be expected this method is extremely computationally expensive since the opacities are recalculated at each step of the simulation. Thus, this feature should only be employed for materials in the system that are truly not in local thermodynamic equilibrium and for which precise frequency-dependent opacities can make a difference in the final temperature and density distributions. For each material in the simulation, there is the option of DCA (Detailed Configuration Accounting) or non-DCA mode. If DCA mode is selected for the material, then the frequency-dependent opacities are calculated based on the atomic level populations at each time-step. If the material is labeled as non-DCA, however, then the opacities are read from a multigroup opacity table generated by *Propaceos*.

Propaceos (Prism Opacity and Equation of State) computes the multigroup opacities (line and continuum) for a material. The multigroup characteristic of these opacities refers to an average opacity calculated for groups of frequencies. That is, groups of frequencies are placed into bins, and a single opacity (absorption or emission) is calculated for that entire frequency bin or group. These group opacities are calculated using the equations

$$\sigma_g^{PA} = \frac{1}{\rho} \frac{\int_{x_g}^{x_{g+1}} B_\nu(T)\kappa_\nu \, dx}{\int_{x_g}^{x_{g+1}} B_\nu(T) \, dx} \tag{2.24}$$

$$\sigma_g^{PE} = \frac{1}{\rho} \frac{\int_{x_g}^{x_{g+1}} \eta_\nu \, dx}{\int_{x_g}^{x_{g+1}} B_\nu(T) \, dx} \tag{2.25}$$

where σ_g^{PA} and σ_g^{PA} are the density-scaled average absorption and emission opacities respec-

tively of group g in units of (cm^2 g^{-1}), κ_ν is the absorption coefficient in units of (cm^{-1}), η_ν is the emission coefficient in units of (ergs s^{-1} Hz^{-1} cm^{-3} sr^{-1}), $B_\nu(T)$ is the Planck function for a blackbody of temperature T (K) in units of (ergs s^{-1} Hz^{-1} cm^{-2} sr^{-1}), and dx is a differential interval in frequency (Hz) space. These equations are simply averages that weight the opacity at each frequency by the continuum emission at that frequency. The motivation for using a weighted average is that the average opacity over a frequency interval will be best approximated by those opacities at frequencies of greatest emission.

The calculation of group opacities can be done under conditions of either local thermo-dynamic equilbrium (LTE), for which the atomic level populations are completely determined by the plasma temperature via the Boltzmann and Saha questions, or non-LTE, for which atomic level populations are computed using atomic rate equations. Note that while *Helios* would include terms for photoionization and photoexcitation in these rate equations, *Propaceos* does not include an external radiation field in its calculation, so these terms are neglected when calculating atomic level populations in non-LTE mode.

Also notice that for a condition of LTE, every process should be balanced by its inverse (see Section 2.2.3 for a more complete discussion of thermodynamic equilibrium), so the *Kirchhoff-Planck relation*,

$$\eta_\nu = \kappa_\nu B_\nu(T) \tag{2.26}$$

should hold (7). In this case, then, there is one opacity which defines each group, since substituting the *Kirchhoff-Planck relation* into either Eq. 2.24 or Eq. 2.25 yields $\sigma_g^{PA} = \sigma_g^{PE}$. For non-LTE, it is not the case that every process is balanced by its inverse (i.e. there is not one temperature that defines the group), so strictly speaking it is assumed that $\sigma_g^{PA} \neq \sigma_g^{PE}$. This is important to mention because these opacities set the radiative cooling and heating rates of the plasma, so for non-equal opacities there will be a net change in energy associated with the frequency group.

Propaceos outputs tabular data of the frequency dependent opacities for a range of temperatures and densities specified by the user. This tabular data can then be read into a hydrodynamics simulation if a material is specified as non-DCA. Shown in Fig. 2.13 is a plot of the opacity data for both neon, the gas cell fill, and mylar, the window material for a single temperature and density. Note that a single opacity *spectrum* is shown for each material, indicating that both calculations employed LTE mode.

2.2.2. Ion Temperature and Mass Density Output

At each time-step in the simulation, *Helios* numerically calculates solutions to the differential (mass, momentum, energy) conservation equations discussed previously. The result of
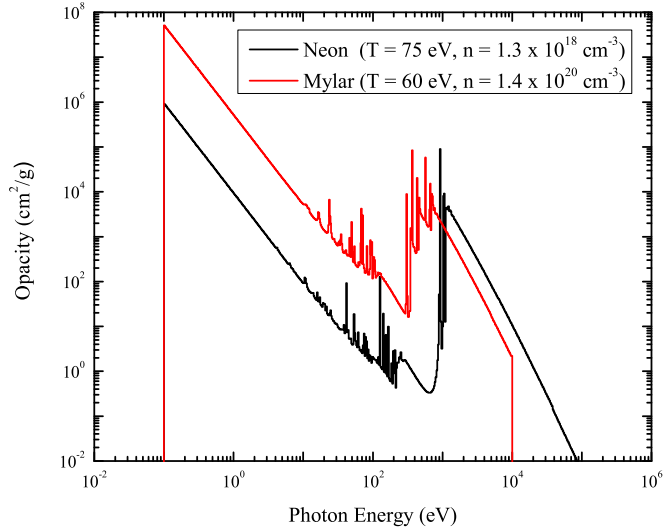
Fig. 2.13.— Frequency dependent Planck opacity data for Neon and Mylar. Both opacity *spectra* were calculated assuming local thermodynamic equilibrium, as evidenced by the single curve for each (recall that only under conditions of LTE does the emission opacity equal the absorption opacity).

these numerical solutions are values for the dependent system variables (e.g. electron or ion temperature, electron or ion density, radiation temperature, fluid velocity, plasma pressure, etc...) in terms of each of the independent system variables (mass, radius, and zone) at each time-step of the simulation. Two such dependent system variables that are of special interest to us are temperature (either electron or ion, since we are using a single temperature model – by convention, we normally plot ion temperature) and mass density as functions of the independent system variable radius. The reason why these system variables are especially important is that the temperature and density distributions will have the most pronounced effect on the synthesized spectrum. Of course, the other dependent system variables also play a role in determining the nature of the synthesized spectrum, but temperature and density are especially important because they set the ionization balance and level populations. Further, the temperature and density distributions are also good measures of how uniform the plasma heating process is and of the degree to which the gas plasma is moving around the cell. Ideally, we would like to have fairly uniform heating and minimal hydrodynamic motion, because no doubt these effects are negligible, or at the minimum different, in the

cosmic scenario of cool circumstellar gas surrounding a high energy x-ray source.

Shown in Fig. 2.14 are the ion temperature and mass distributions for a representative non-LTE calculation. Notice that since the user can set *Helios* to output system variable data for multiple time-steps, it is possible to overplot the distributions for different times in the simulation and compare how the distributions change with time. If one outputs for many time-steps, it is possible to construct a three dimensional plot of the ion temperature (and mass density) as a function of both position and time. Such a 3-D plot is shown in Fig. 2.14(c).

2.2.3. Non-LTE vs. LTE

In general, a closed system is said to be in *thermodynamic* or *thermal equilibrium* if there is no net flow of energy through that system. As an example, consider a box filled with gas. If we think of this system as containing both gas particles and radiation (in the form of photons), then our requirement for thermodynamic equilibrium is that there is no net flow of energy between the particles, and no net flow between the gas particles and the ambient radiation field in the box. The most simple example of such a system would be one at absolute zero, where the particles are not moving and are not emitting any radiation (since they have no energy). It is possible, however, to achieve thermal equilibrium for a temperature other than absolute zero, as long as you thermally insulate or close the system. In such a system, the temperature is held uniform because every process that could change the energy distribution, like the emission of a photon, is balanced by its inverse process, in this case the absorption of a photon. This process/inverse process balance is also true for the particles themselves. For a given uniform gas temperature the particles are characterized by a specific distribution of velocities known as the Maxwell-Boltzmann distribution. Now, for any collision in which the kinetic energies of any particles pair are changed, there is another collision of a second pair of particles of initial kinetic energies equal to the final kinetic energies of the first pair which results in second pair having kinetic energies equal to the initial kinetic energies of the first pair. In other words, collisions occur and energy is transferred between particles, but overall for the system the velocity (or energy, since $KE = \frac{1}{2}mv^2$) distribution is conserved for a system in thermal equilibrium.

Of course, closed systems in thermodynamic equilibrium are idealizations, because practically speaking it is never possible to fully isolate a system from its surroundings. Though, we can approximate a condition of thermal equilibrium for a system if the distance over which the temperature changes is large compared to the distance over which a particle or photon collides with another particle (known as the *mean free path*). This approximate condition of thermal equilibrium is known as *local thermodynamic equilibrium* (LTE), and is a

valid approximation for a region of nearly constant temperature in which the photons and particles contained in the system cannot escape (because they collide with another particle first).

Relevant to our investigation is the determination of whether the gas in the cell is in LTE. Certainly, it would seem that as long as the gas in the cell is bombarded from one side by a high energy density flux, there will be a non-zero net flow of energy through the system (since the temperature of the gas closest to the pinch will be higher than the temperature of the gas farther from the pinch). It is possible that the net flow of energy will tend toward zero both for early times when the pinch emission is negligible and for late times when the pinch has turned "off" after its peak emission, but the features (absorption and emission) for a time-integrated spectrum will be dominated by the state of the gas at the peak of the pinch emission rather than early or late pinch emission at the beginning or end of the experiment respectively. Thus, in trying to accurately model the hydrodynamic evolution of the gas in the cell, we are much more concerned with what the gas is doing at or around the peak pinch emission than we are with what it is doing at then end (or beginning) of the experiment.

Assuming that the part of the experiment in which we are most interested is not well approximated by LTE, it then becomes necessary to track the atomic rate equations at each time step of the simulation. For a uniform electron temperature set by LTE, the level populations are set by the Boltzmann (for excited states) and Saha (for ionization states) equations. However, for our case where the temperature is not uniform over a distance significantly larger than the mean free path, there is not a single temperature we can use to calculate the level populations from the Saha and Boltzmann equations. Instead, for a non-LTE calculation, *Helios* calculates the level populations at each time step by solving a set of multi-level atomic rate equations. This modification can make a significant difference in the calculated temperature distribution, as shown in Fig. 2.15.

The nature of the uncertainty of the thermodynamic condition of the gas cell plasma is the uncertainty in the degree of photoionization of the plasma. While it is never the case that a plasma is completely photoionized or coronal, there are plasmas for which these labels are appropriate because their ionization balance is dominated either by photoionization or collisional processes. The gas cell plasma, however, seems to be somewhere in the middle, having neither photoionization nor collisonal processes dominate its ionization balance. If we associate the condition of LTE with a coronal plasma (since collisions dominate, implying that the mean free path is short) and the condition of non-LTE with a photoionized plasma (since collisions are less frequent for a cooler plasma, implying a longer mean free path), then as the degree of photoionization of the plasma increases, the need for a non-LTE calculation also increases.
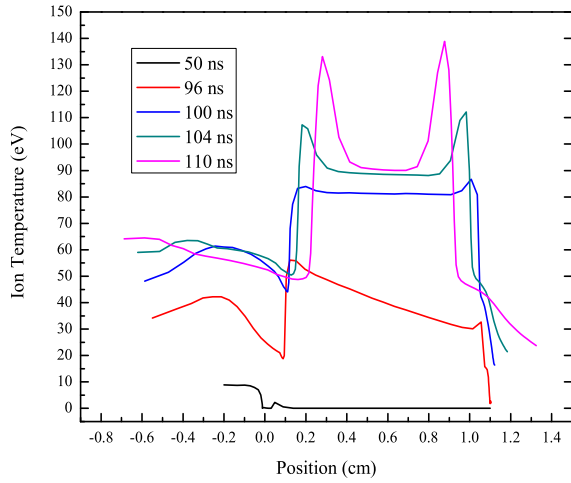
(a)
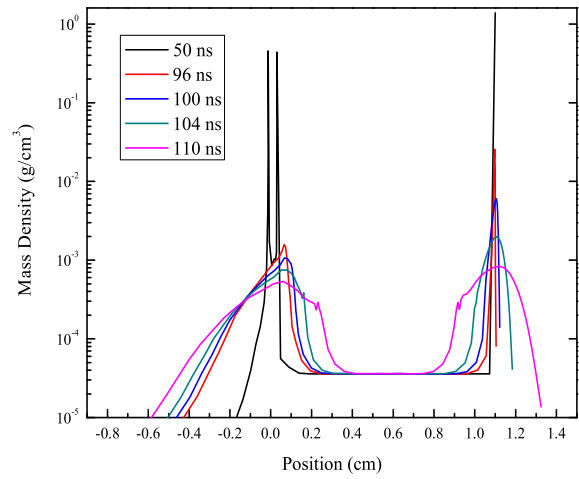
(b)
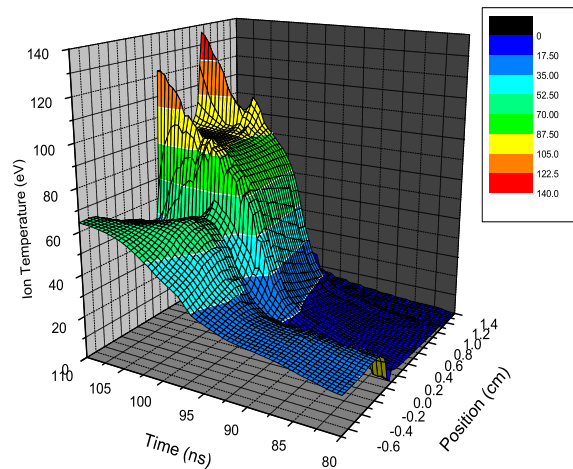
(c)

Fig. 2.14.— (a) Ion temperature as a function of position for several times in the hydro simulation, (b) mass density as a function of position for several times in the simulation, and (c) a 3-D plot of ion temperature as a function of position and time. For all three plots the radiation flux from the pinch is incident from the left (negative position values). Notice the radiation wave evidenced by the temperature gradient in (a) and (c) for simulation times immediately preceding the peak of pinch emission at $t = 100$ ns. Also notice the shock (or compressional) heating of the gas in the cell near the mylar windows due to their (the mylar windows') collapse.
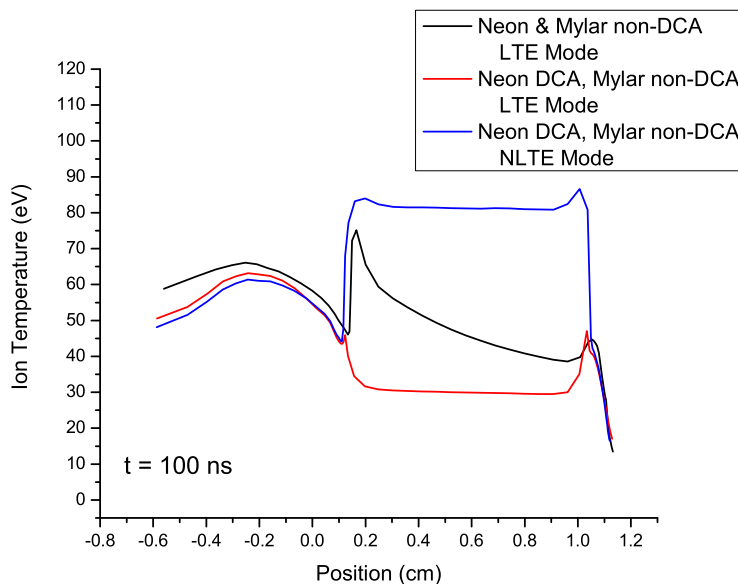
Fig. 2.15.— Comparison of ion temperature distributions at $t = 100$ ns for three independent simulations. Notice that in non-LTE mode, *Helios* calculates a higher average ion temperature at the peak of the pinch emission. The DCA label (Detailed Configuration Accounting) for each material in the simulation refers to how the opacities of each material are calculated. If a material is labeled as non-DCA, then multigroup opacities are used from a *Propaceos* data table. Otherwise, if a material is labeled as DCA, then frequency-dependent opacities are calculated based on the atomic level populations at each time-step. These populations can be calculated using either a LTE or a non-LTE model.

2.3. Spect3D

The final step of the simulation procedure is the synthesis of a spectrum (either absorption or emission, which correspond to different lines of sight) which can be compared to a measured spectrum from the actual experiment. This modeling component has two distinct steps: (1) construct an atomic model for relevant energy levels with radiative and collisional cross section data, and (2) using the atomic model, density and temperature distributions from the hydrodynamics simulation, and external radiation field from the viewfactor simulation, an absorption or emission spectrum is synthesized. For the first modeling component of this synthesis procedure, the program called *Atomic Model Builder* is used, and for the second the program called *Spect3D*.

2.3.1. Atomic Model Builder

Atomic Model Builder, as its name implies, is a program used for constructing atomic models. This program does not have the capability to compute elemental collisional and radiative cross sections, so it requires this data as an input. For our simulations, we used ATBASE data files for the relevant elements in the gas cell experiments. Once read the ATBASE file is read into the program, constructing the atomic model reduces to the task of selecting which atomic levels should be included in the calculation of atomic populations of excited and ionization states. Ideally, we would select all energy levels of the atom included in the ATBASE data file, but this would be computationally expensive and is not necessary if we are only concerned with certain spectral features as diagnostics. If, for example, the spectral features in our measured experimental spectrum are dominated by He-like Ne (Ne IX), then it is not absolutely necessary to include all energy levels of O-like Ne (Ne III). In fact, it is sufficient to select only the ground state for those ionization states in which we are unconcerned. Shown in Table 1 are the atomic models used for modeling the gas cell experiments. The Ne model is used for the gas fill of the cell, and the H, C, and O models are used for the mylar windows (since we assume mylar to be composed of H, C, and O in the proportions 36.4%, 45.5%, and 18.2% respectively by mass). Notice that we have only selected the ground states for all of the ionization states of H, C, and O (or the mylar) since the spectral features of those elements are not used as diagnostics of our modeling procedure.

2.3.2. Absorption and Emission Spectra

Once the atomic models of the elements are constructed, then the second stage of the spectral synthesization process can begin. Like *Helios*, *Spect3D* supports several different

Table 1: Atomic Models

Neon

Ionization State	No. of Levels
Ne I	1
Ne II	1
Ne III	1
Ne IV	1
Ne V	1
Ne VI	1
Ne VII	1
Ne VIII	264
Ne IX	223
Ne X	22
Ne XI	1

Hydrogen

Ionization State	No. of Levels
H I	1
H II	1

Carbon

Ionization State	No. of Levels
C I	1
C II	1
C III	1
C IV	1
C V	1
C VI	1
C VII	1

Oxygen

Ionization State	No. of Levels
O I	1
O II	1
O III	1
O IV	1
O V	1
O VI	1
O VII	1
O VIII	1
O IX	1

modes of computation related to opacity models and their associated conditions of thermo-dynamic equilibrium. The simplest of these modes uses the multi-group opacity data from a *Propaceos* opacity model. Not surprisingly, this mode is least computationally expensive of all of the computation modes, but is also the roughest approximation to the actual situation, since the *Propaceos* data assume LTE[5] and are the binned average opacities (average opacities computed for ranges of frequencies).

The other two computation modes are slightly more rigorous than the first in that they resolve the line and emission opacities for all wavelengths instead of computing the average opacities over frequency bins. Both of these modes compute the opacities at run-time, but the two differ in their method of calculating these opacities because they make different assumptions for the thermal condition of the plasma. The simpler of the two modes assumes LTE, for which the atomic level populations are completely determined by the Saha and Boltzmann equations, while the more rigorous mode assumes non-LTE, for which atomic level populations are determined by solving atomic rate equations for each time-step in the simulation. This final computation mode is known as a *collisional-radiative* level population model, which can include both collisional and radiative processes (i.e. both coronal and photoionization processes). For our simulations, the following processes were included in the

---

[5]As mentioned in Section 2.2.1, *Propaceos* supports both LTE and non-LTE calculations of the multigroup opacities, but for the purposes of our simulations, all *Propaceos* files assume a condition of LTE.

atomic rate equations at each time-step of the simulation:

(1) Collisional Excitation/Deexcitation;

(2) Spontaneous Emission;

(3) Photoexcitation/Stimulated Emission;

(4) Radiative Recombination;

(5) Collisional Ionization/Recombination;

(6) Autoionization/Dielectronic Recombination;

(7) Photoionization/Stimulated Recombination.

One can think of each of these processes as representing a term on either side of an ionization balance equation like Eq. 1.1. This equation can then be used to solve for the ratio of atomic level populations (the ionization balance) as a function of the rates of these atomic processes alone. The atomic models constructed in *Atomic Model Builder* contain the relevant elemental collisional and radiative cross sections from ATBASE data files, and the external radiation field necessary to compute the rates for photoionization processes is taken from the *VisRad* viewfactor simulation ouput.

Once the frequency and time-dependent opacities are determined, all that is further required to synthesize an absorption spectrum is the definition of a backlighting spectrum. For these simulations, we implement a blackbody continuum backlighter source of temperature $T = 500$ eV, since that spectrum serves as a good approximation of the pinch spectrum at the wavelengths of interest. Of course, an emission spectrum does not require a backlighter for spectral synthesis, so once the atomic level populations are determined, the emission coefficient (the emission *opacity* multiplied by the mass density) immediately follows. The frequency dependent emission coefficient fully determines the emission spectrum, since for pure emission

$$dI_\nu = \eta_\nu \, ds \qquad (2.27)$$

where dI_ν is the emergent intensity (erg s^{-1} cm^{-2} Hz^{-1} sr^{-1}) at frequency ν (Hz), η_ν is the
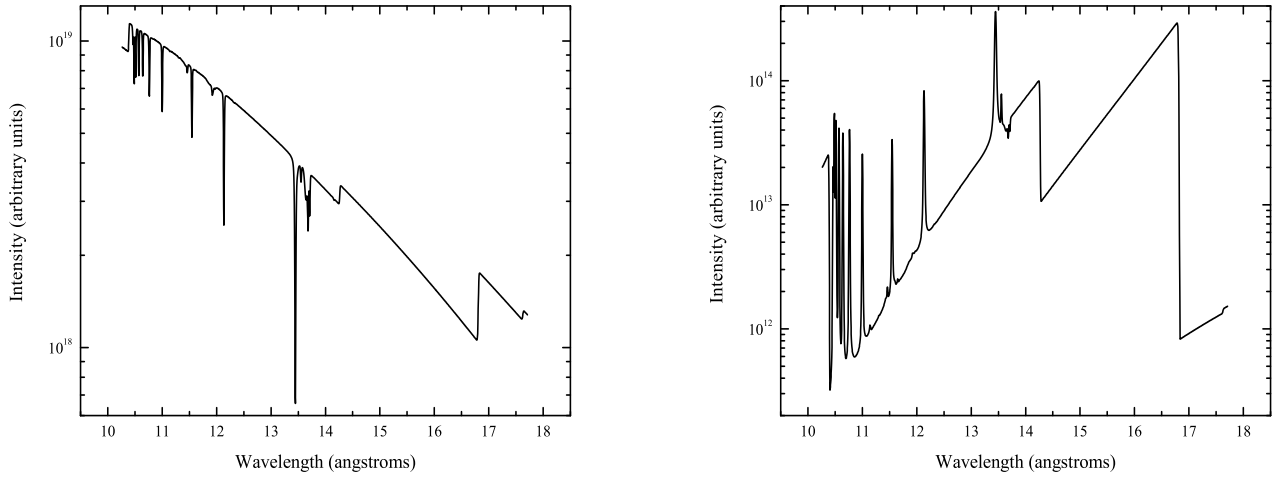
(a)   (b)

Fig. 2.16.— Time-resolved synthesized (a) absorption and (b) emission spectra for $t = 100$ ns. The continuum backlighter for the absorption spectrum is a blackbody of temperature $T = 500$ eV, which approximates the pinch spectrum at these wavelengths.

emission coefficient (erg s^{-1} cm^{-3} Hz^{-1} sr^{-1}) at ν, and ds is distance over which a particular emission coefficient is defined. Fig. 2.16 shows an example absorption and emission spectrum synthesized using *Spect3D*.

3.   Modeling of Shot Z543

The previously conducted experiment we chose to model was one for a ride-along gas cell on a Z-machine shot described internally at Sandia National Laboratories as Z543. In (1) Bailey describes the parameters of the experimental setup for this shot. The gas cell had dimensions 1 cm $\times$ 2 cm $\times$ 2.34 cm, with the 1 cm dimension oriented along the line of sight, and the 2.34 cm dimension perpendicular to the the anode insert. The cell had windows on three sides (two surfaces perpendicular to the line of sight and one surface parallel to the line of sight and perpendicular to the anode insert) composed of mylar and of thickness 1.5×10^{-4} cm. The radial distance from the pinch axis to the *front* mylar window was 5.7 cm, and the gas fill of the cell was neon of particle number density 1.06×10^{18} cm^{-3}.

Pictured in Fig. 3.1 are photographs of the *anode insert/current return can* and the *wire array* for shot Z543. Notice in the *anode insert/current retun can* image that there are two depression rings in the anode insert. The gas cell (not shown) was placed along one of the indicated lines of sight (labeled LOS in the photograph) in the outer depression ring. This location was chosen as a compromise between maximizing the flux of radiation hitting the cell and maintaining the relative uniformity of flux hitting different portions of the face of the gas cell.

Also reported by Bailey in (1) were the total x-ray energy (1.45×10^6 J), peak power (135×10^{12} W), and full-width at half-maximum burst pulse (7.5 ns) of shot Z543. Using the above information, along with the measured time-dependent pinch power and radius, we implemented our modeling procedure to produce a synthesized absorption spectrum which could be matched to the measured absorption spectrum from the experiment. The parameters of each simulation are listed in Tables 2 - 4, and the results of each stage of our modeling procedure are shown in Fig. 3.2 - 3.4.

– 49 –
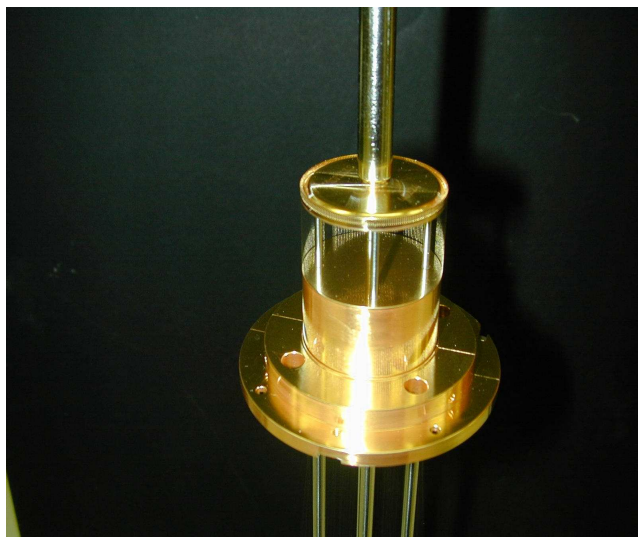
(a)   (b)

Fig. 3.1.— Photographs of (a) the anode insert and current return can through which the current pulse passes after being driven through the Z-pinch wire array, and (b) the tungsten wire array, both from shot Z543.

Table 2: VisRad Simulation Parameters

| OBJECT	Outer Apron	Cover	Current Return Can	Bottom Flange	Top Flange	Floor	Gas Cell	Pinch
POSITION								
r (cm)	0	0	0	0	0	0	5.65	0
z (cm)	-0.85	1	0	-0.85	0.85	-1.0	0.77	0
phi(deg)	0	0	0	0	0	0	0	0
polar	0	0	0	0	0	0	90	0
azimuthal	0	0	0	0	0	0	0	0
rotation	0	0	0	0	0	0	0	0
SIZE/ GRIDDING								
size (cm)	$r_{min} = 3.32$ $r_{max} = 7.0$	$r_{min} = 0$ $r_{max} = 2.0$	$r = 2.5$ $h = 2.0$	$r_{min} = 2.5$ $r_{max} = 3.32$	$r_{min} = 2.5$ $r_{max} = 3.32$	$r_{min} = 0$ $r_{max} = 2.5$	$l = 2.0$ $w = 2.0$	r varies $h = 1.98$
min. angle	0	0	0	0	0	0	...	0
max. angle	360	360	360	360	360	360	...	360
radial grid points	4	10	10	10	10	10	6	10
azimuthal grid points	18	18	18	18	18	18	6	18
surface normals	up	down	in	up	down	up	down	out
MATERIAL PROPERTIES								
albedo	variable	variable	variable	variable	variable	variable	0.5	0.7
power (TW)	0	0	0	0	0	0	0	variable
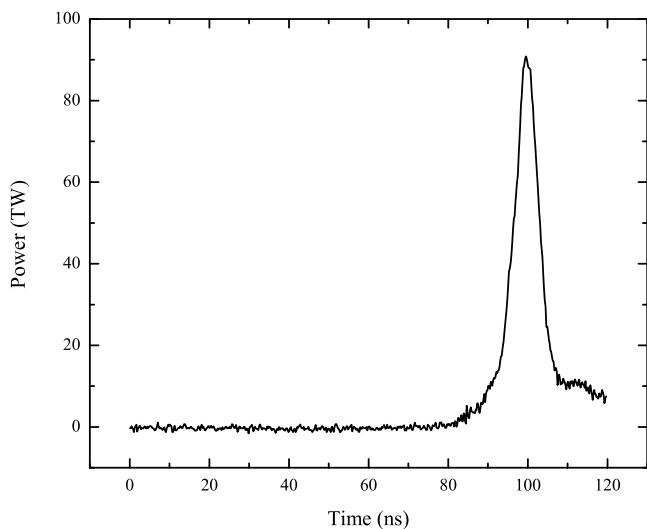
(a)
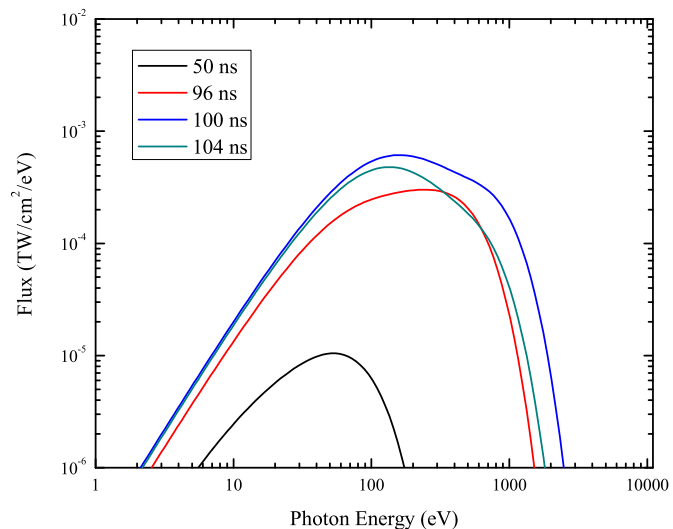
(b)

Fig. 3.2.— Time-dependent (a) pinch power and (b) incident flux at the center of the face of the gas cell. The variable albedo model for the surfaces in this simulation came from Rochau (15) and is plotted in 2.6 for the "three" main surface types: anode insert (outer apron), current return can (current return can, bottom flange, top flange), and glideplane (floor, cover). As expected and shown in the time-dependent spectrum, the largest flux incident on the gas cell occurs at the peak of the pinch emission at $t = 100$ ns, and also that, as explained earlier, the incident flux after the peak emission is not the same as the incident flux before the peak emission because the pinch is actually emitting more flux at the later time despite having the same power output.

Table 3: Helios Simulation Parameters

SPATIAL GRID									
Region	R_{min}	R_{max}	DCA Material	Thickness	Mass Density	Number of Zones	Mean Atomic Weight	Temperature	Velocity
	(cm)	(cm)		(cm)	(g/cc)		(amu)	(eV)	(cm/s)
mylar1	0.0	0.00014	no	0.00014	1.39	20	8.735	0.025	0.0
neon	0.00014	1.10014	yes	1.1	3.6×10^{-5}	20	20.18	0.025	0.0
mylar2	1.10014	1.10028	no	0.00014	1.39	20	8.735	0.025	0.0

ATOMIC PROCESSES (Non-LTE)					
Collisional Excitation/ Deexcitation	Spontaneous Emission	Photoexcitation/ Stimulated Emission	Radiative Recombination	Collisional Ionization/ Recombination	Autoionization/ Dielectronic Recombination	Photoionization/ Stimulated Recombination

OTHER SETTINGS					
Minimum Temperature for CR (eV)	Points in Continuum	Additional Points Per Line Transition	Radiation Transport Model	Frequency Groups	Energy Model
10	200	15	Multiangle (2)	50	$T_i = T_e$
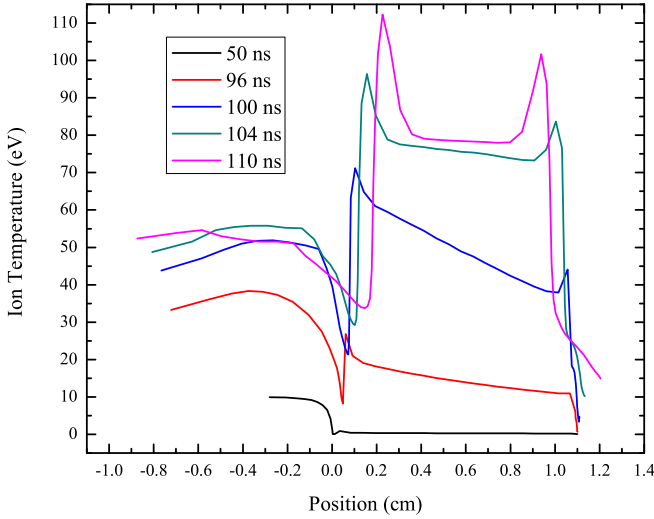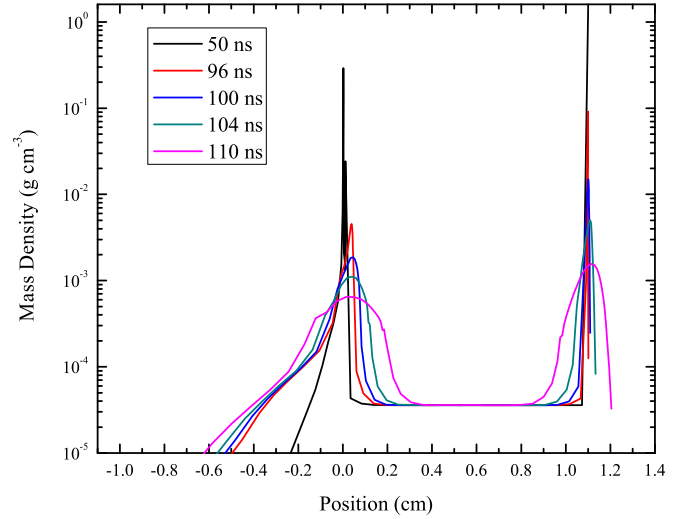
(a)   (b)

Fig. 3.3.— (a) Ion temperature and (b) mass density as functions of position for several times in the hydrodynamics simulation. This simulation was nearly a fully non-LTE calculation, except for the classification of the two mylar windows as non-DCA materials. As discussed in section 2.2.3, high density plasmas imply more collisions and a shorter mean free path, in which case LTE is an appropriate approximation to make. The ion temperature plot shows that the radiation incident from the left heats up and ablates the mylar. This ablation process spreads the mylar out, leaching it in the direction of both the pinch and gas in the cell. As the mylar moves toward the center of the gas cell, a shock front is formed along which the neon is heated drammatically. This shock heating is evidenced by the spikes in temperature at the front and back of the gas cell. Fortunately, there remains a central portion of the cell isolated from the boundary effects where conceivably a plasma could be dominated by photoionization processes. This simulation also shows that there is a temperature gradient across the gas cell for much of the simulation, including when the pinch reaches its peak emission. This gradient evidences a radiation wave propagating through the gas, indicating a non-zero flow of energy through the cell and a non-equilibrated thermodynamic condition. The mass density plot also shows the ablation of the mylar in the form of a sharp density distribution of mylar (at the front and back of the gas cell) spreading out as time progresses.

Table 4: Spect3D Simulation Parameters

MATERIALS					
	DCA Material	Mean Atomic Weight (amu)	Element Number	Element Symbol	Number Fraction
mylar	yes	8.735	1	H	0.364
			6	C	0.455
			8	O	0.182
neon	yes	20.18	10	Ne	1.00

KINETICS MODEL				
DCA Level Population Model	Photoexcitation Model	Photoionization Model	Points in Continuum	Additional Points Per Line Transition
Collisional-Radiative	Non-Local Radiation Radiation (1-D Planar or Spherical)	Non-Local Radiation Radiation (1-D Planar or Spherical)	200	15

DETECTOR										
Position (cm)			Center of Projection (cm)			Pixel Count		Pixel Spacing		Projection	Vertical Alignment	XRD Resistance (ohms)
X	Y	Z	X	Y	Z	HORIZ.	VERT.	HORIZ.	VERT.	Orthographic	Z-Axis	50
1.0	1.0	1.0	0.0	0.0	0.0	1.0	1.0	0.05	0.05			

OTHER SETTINGS				
Hydrocode File Type	CR Simulation Type	Geometry	Plasma Grid Type	Backlighter Spectral Type
EXODUS	Steady-State	1-D	Absolute (Lagrangian)	Continuum T = 500 eV
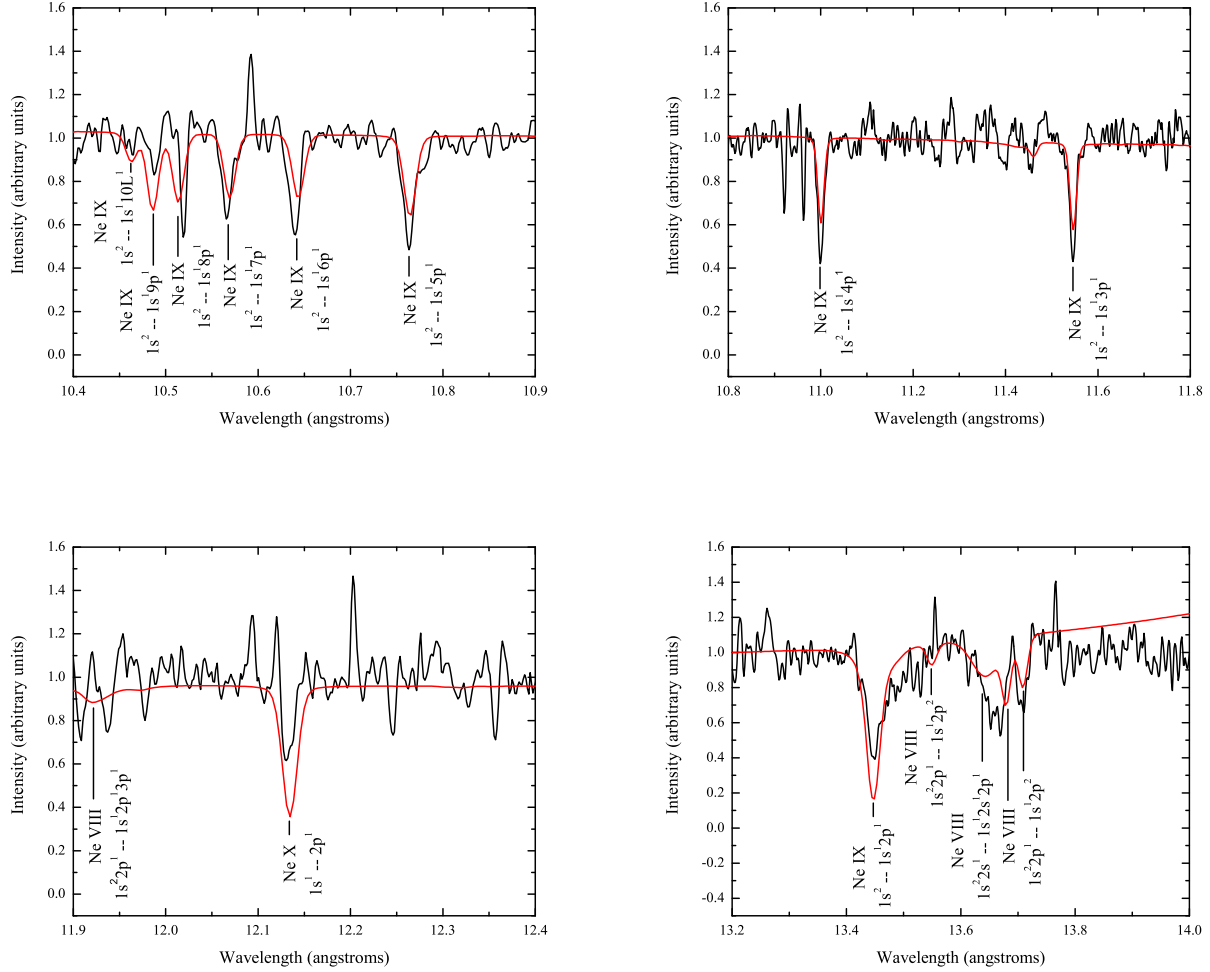
Fig. 3.4.— Multiple frames showing different wavelength intervals of a Spect3D synthesized spectrum (red) matched to the measured time-integrated spectrum from Shot Z543 (black). The spectral resolution of the synthesized spectrum is $E/dE = 800$. There is some disagreement between the two spectra with regard to the strength of the lines, which can be diagnosed by looking at specific line transitions. The Lyman α line in the bottom left frame is much deeper in our model spectrum than in the measured spectrum, indicating that our modeled plasma is too ionized (or too hot) as compared to the actual plasma in the experiment. Other lines corroborate this conclusion, including the He-like lines in the two top panels that are too shallow in our model, indicating that the density of He-like Ne is too low, or that overall the gas is too ionized. Also notice that the wavelengths of the lines for the He-like excitations to higher energy quantum states (from the ground state to $n = 6, 7, 8, 9, 10$) do not correspond exactly. This disagreement seems to indicate that there may be something wrong with the fundamental physics used to calculate the wavelengths of the line transitions.

4. Scaling Studies

As mentioned at the end of Section 1.6, the gas plasma created in past gas cell experiments on the Z-machine has been photoionized to a degree much less than that of the cosmic photoionized plasmas in which we are interested. From Eq. 1.3 we see that there are three ways to boost the ionization parameter: [1] increase the luminosity of the x-ray source, [2] decrease the distance r from the x-ray source, and [3] decrease the particle number density of the gas. [1] is not a good candidate for a scaling study, since although it is quite possible that future experiments will have higher luminosity x-ray sources, that is not something we can necessarily expect nor can we precisely predict what the new luminosity might be. [2] is not a terribly interesting candidate for a scaling study because there are practical limitations on where the gas cell can be placed in these experiments. As shown in Fig. 3.1, there are two depression rings on the anode insert on which experiment specific apparatus can be placed. In past experiments the gas cell has been placed in the outer depression ring, so future experiments could boost the ionization parameter by placing the cell on the inner depression ring (at the risk of increasing the temperature gradient across the cell and bulk hydrodynamic motion within the cell). Certainly, the results of a simulation modeling an experiment with the gas cell at this new location would be both interesting and insightful, but given that this location is the only other choice (aside from the previous location) for the position of the gas cell in future experiments, [2] is not a good candidate for a scaling study because it does not provide us with a large range of possible values for the scaled experimental parameter.

Thus, we are left with [3] as the best candidate for a scaling study. The density of the gas cell fill is an experimental parameter that can be easily modified, and the range of values available to us is only limited by the minimum density that will yield measurable spectral features. Indeed, the goal of this scaling study is to constrain the value of this critical density by probing how much the density can be decreased before the spectral features in the resultant absorption spectrum either vanish or become too weak to practically distinguish from the noise of the measured spectrum.

A series of simulations were conducted, all identical to the simulation conducted in Section 3 except that the Ne density used in the hydrodynamics simulation was systematically decreased. Shown in Fig. 4.1 are the results of the hydrodynamics simulations for three particle number densities: 5.37×10^{17}, 1.06×10^{17}, and 7.46×10^{16} cm^{-3}. The absorption spectra synthesized for these three densities, as well as for 1.06×10^{18} cm^{-3} (the density employed in shot Z543), are shown in Fig. 4.2.

Notice in Fig. 4.1 that as the density is decreased, the compressional heating from the collapse of the mylar walls penetrates farther into the gas. Though not shown here,

simulations conducted for densities less than $n = 7.46 \times 10^{16}$ cm^{-3} found that for these lower densities the compressional heating penetrates the core of the gas cell, thereby *erasing* any photoionized characteristic of the plasma residing there.

Fig. 4.2 seems to indicate that $n = 7.46 \times 10^{16}$ cm^{-3} is approximately the minimum density that can be used in the gas cell that will still produce measureable spectral features. This density is a factor of 14 less than the density used in shot Z543, so a future experiment identical to shot Z543 except for a Ne gas cell fill density of $n = 7.46 \times 10^{16}$ cm^{-3} should achieve an ionization parameter of ~ 70 erg cm s^{-1}. It should be mentioned, though, that the only two measurable features for this density are the Lyman α line and the He-like line at 13.43 angstroms; the other spectral features are either non-existent at this density or are too weak to distinguish from the noise associated with an experimental spectrum. If we would like more than these two spectral features in our spectrum, then a higher minimum density is required.

Future experiments might employ *heavier* gas fills, such as Ar, because these gases would be able to achieve the same mass density (which sets the degree of penetration of shock heating from the mylar walls) for a smaller particle density (and thus higher ionization parameter).

– 58 –

$$n = 5.37 \times 10^{17} \text{ cm}^{-3}$$
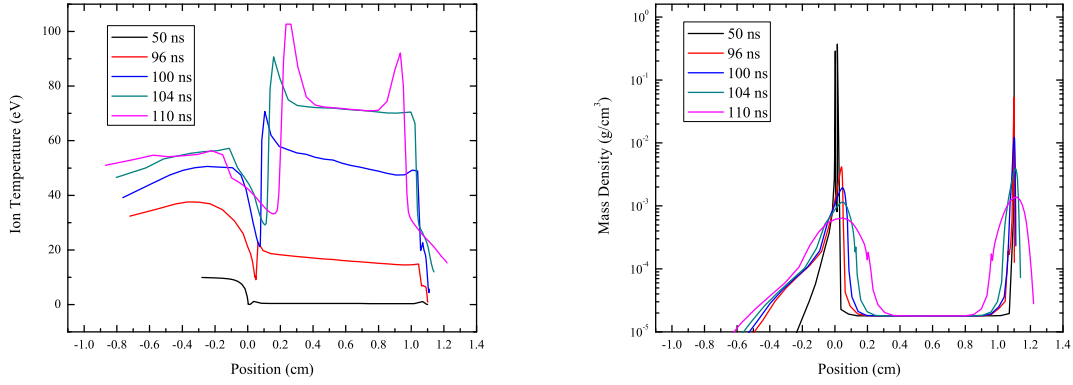
$$n = 1.06 \times 10^{17} \text{ cm}^{-3}$$
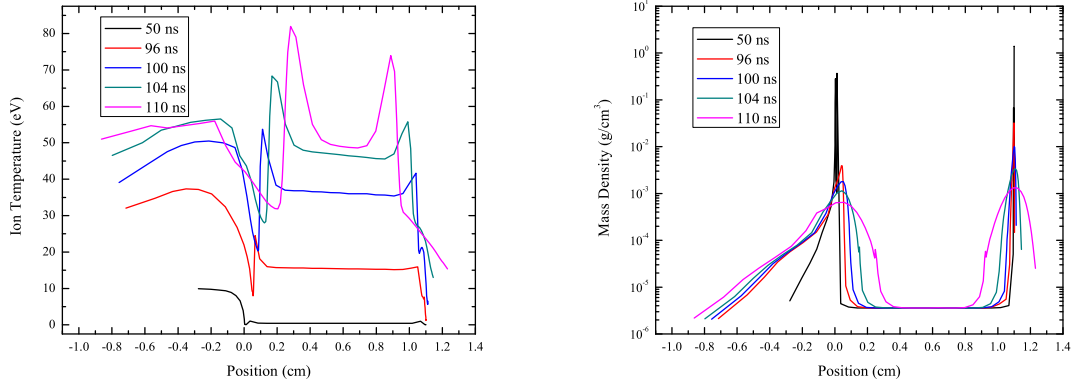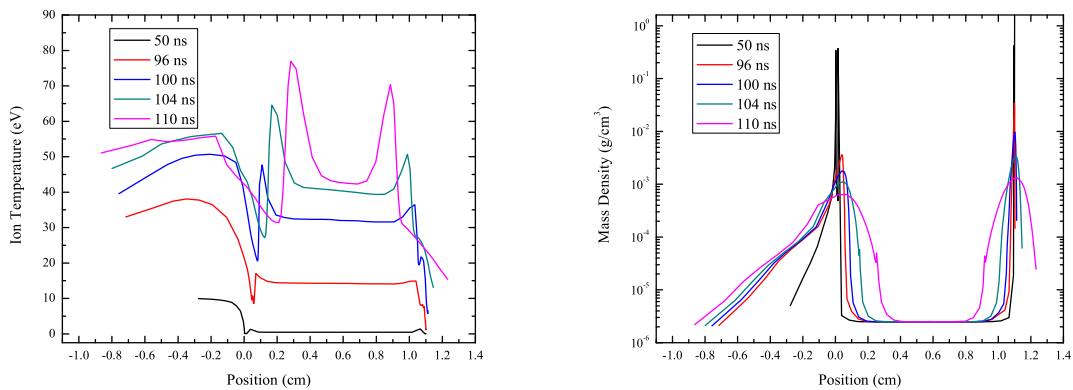

$$n = 7.46 \times 10^{16} \text{ cm}^{-3}$$

Fig. 4.1.— Ion temperature and mass density as functions of position for several times in three hydrodynamics simulations using different gas fill densities.
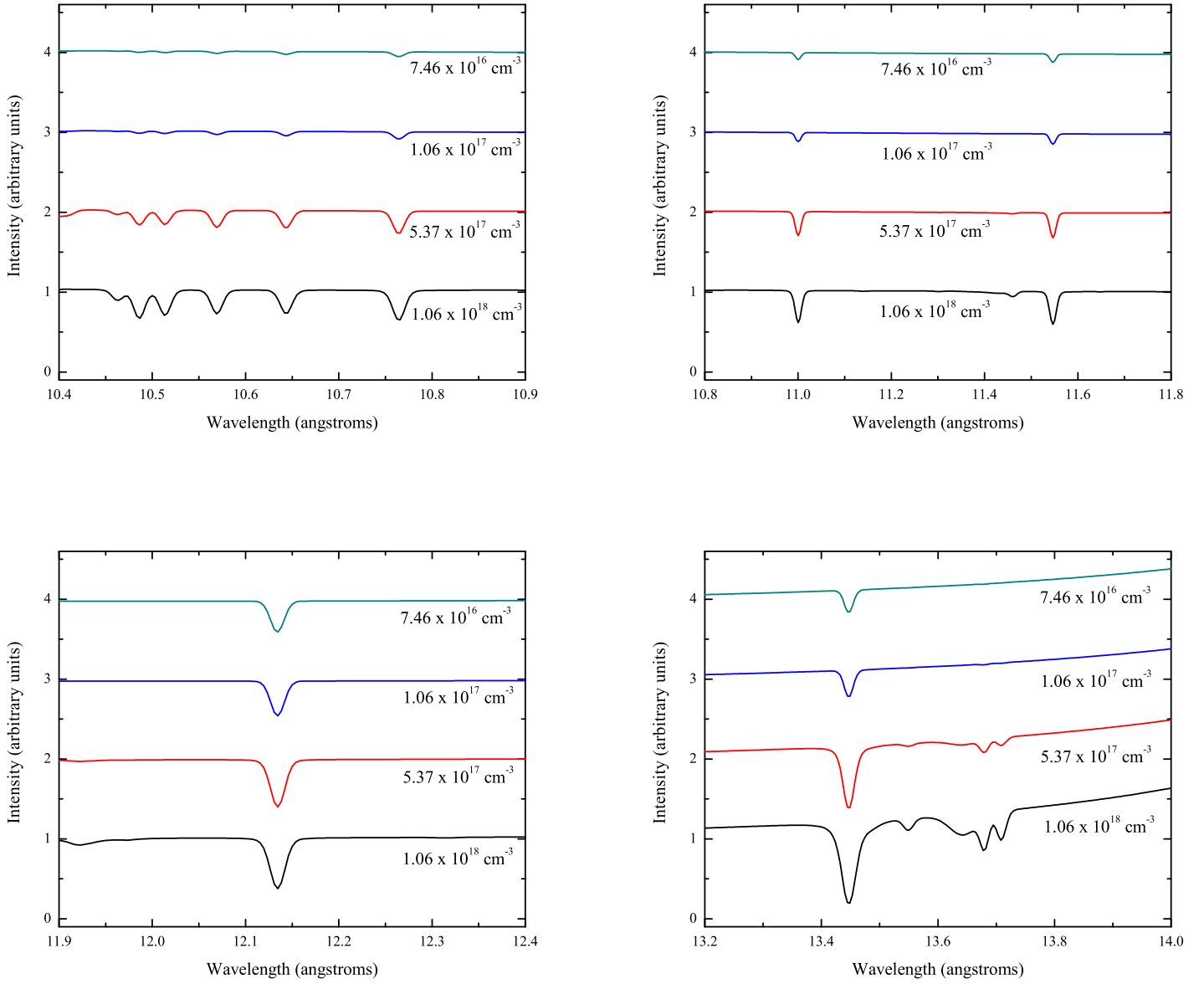
Fig. 4.2.— Multiple frames showing wavelength intervals of time-resolved synthesized absorption spectra at $t = 100$ ns for several different gas fill densities. The backlighter for each spectrum is a blackbody of temperature $T = 500$ eV.

5.   Spectral Diagnostics

The bridge between the modeling procedure and the actual experiment for the gas cell experiments is the measured spectrum. The spectrum measured in the experiment is a diagnostic which we can utilize to determine how well our modeling procedure is describing the actual experiment. The more information contained in the experimental diagnostic, the more effective each diagnostic will be at testing our modeling procedure. Further, the more diagnostics one has the more stringent the test will be for the modeling procedure.

Past experiments have measured only a single time-integrated absorption spectrum, and thus have provided only a single diagnostic that is not an entirely fair test of the time-resolved spectra we synthesize in our modeling procedure. As an approximation, we match the synthesized spectrum at $t = 100$ ns to the measured time-integrated spectrum (since the time-integrated spectrum will be dominated by the spectrum at this time-step because the pinch emission is peaked at that time-step), but certainly there will be discrepancies in the match between the synthesized and measured spectra, even if we are modeling the experiment perfectly.

In future experiments, we plan to make simultaneous time-resolved emission and absorption spectroscopic measurements, which should provide us a more stringent test of our modeling codes. Namely, having spectra for several times in the experiment will allow us to test the accuracy of our model for more than one time-step. Also, having both emission and absorption spectra will allow us to more effectively test how well we are modeling different properties of the experimental plasma. Specifically, an emission spectrum gives us information about the characteristic temperature of the plasma via the widths of the narrow radiative recombination continua (see Fig. 1.3) and an absorption spectrum gives us information about the ionization distribution in the plasma.

Shown in Fig. 5.1 and Fig. 5.2 respectively are time-resolved absorption and emission spectra synthesized from the modeling simulations for shot Z543. These figures seem to indicate that time-resolved spectroscopic measurements in future experiments similar to shot Z543 should be characterized by the weakening of Li-like lines in both absorption and emission and the strengthening of the Lyman α line in emission as time progresses.
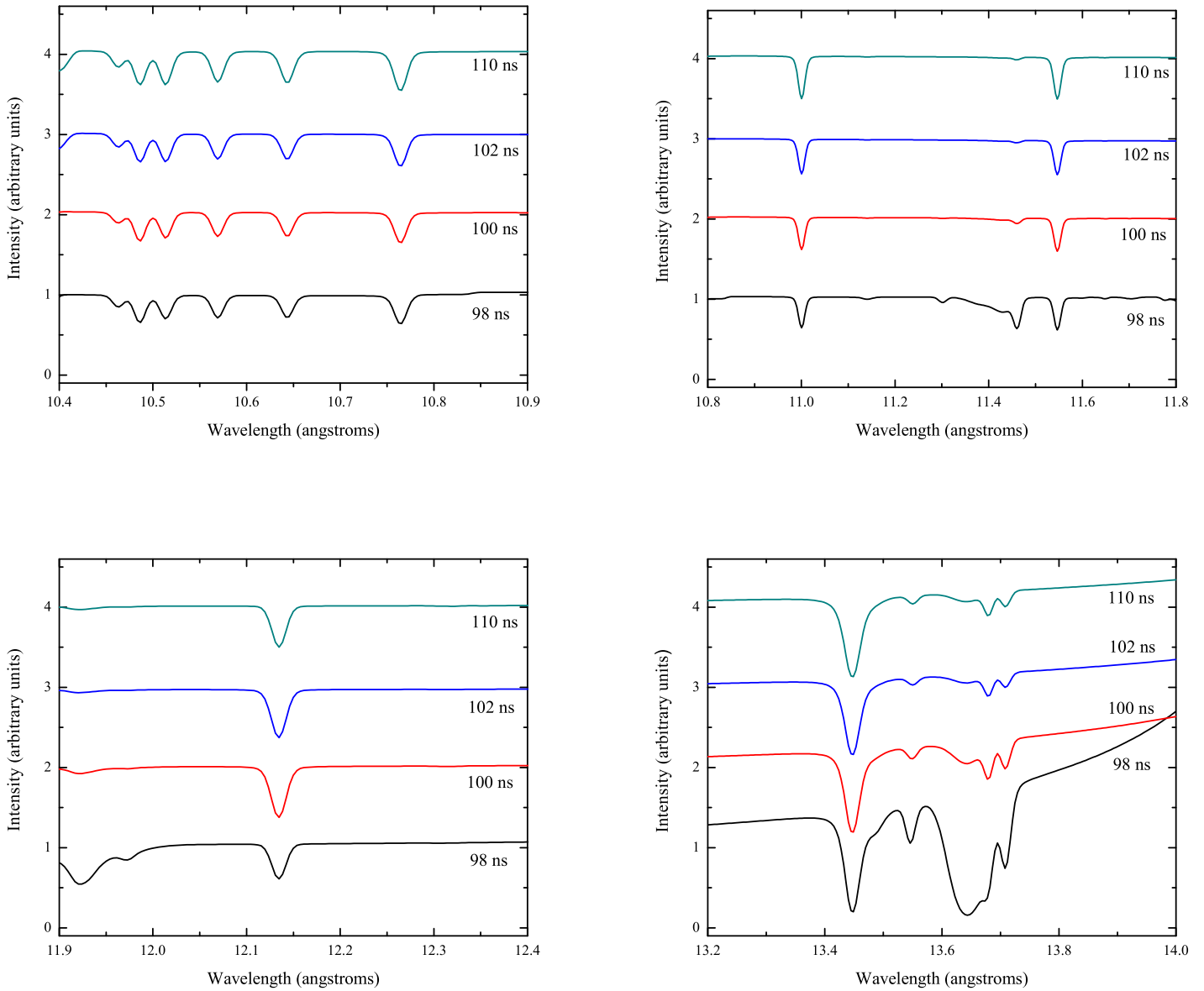
Fig. 5.1.— Multiple frames showing wavelength intervals of a time-resolved synthesized absorption spectrum. Notice that while the strength of most features in each frame remains constant with time, there are certain spectral features that become weaker as time progresses. Namely, the Li-like lines at ∼ 11.93 and ∼ 13.7 angstroms show definitive weakening as time progresses. The strong absorption feature at ∼ 11.46 angstroms does not correspond to any line transition, but it too weakens as time progresses.
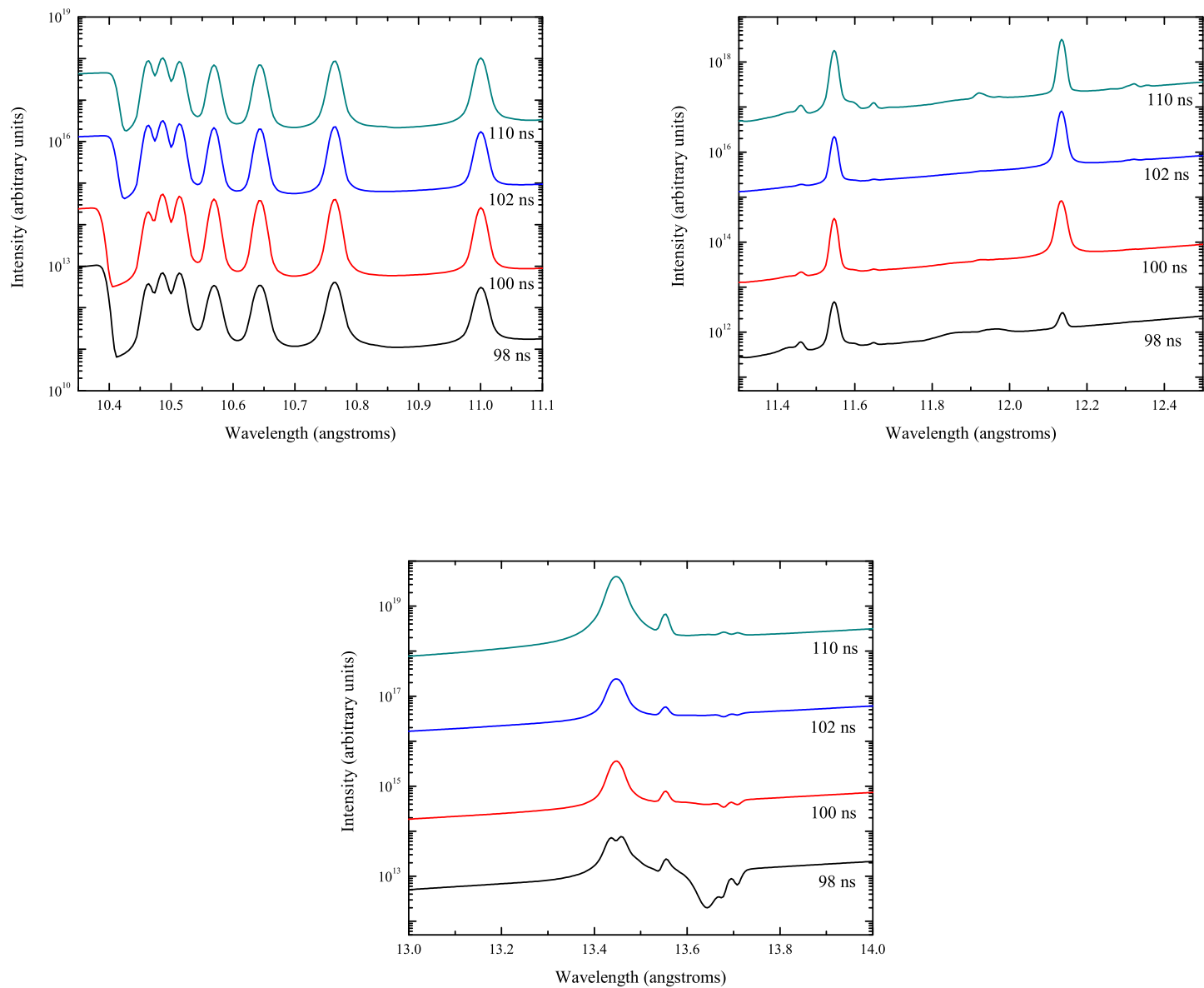
Fig. 5.2.— Multiple frames showing wavelength intervals of a time-resolved synthesized emission spectrum. Notice that the Li- and He-like lines in the top two frames remain fairly constant in strength for different time-steps in the simulation, while the H-like Lyman alpha emission line in the top right frame increases in strength and the Li-like absorption features in the third frame become weaker with time.

6. Conclusions

As established in Section 1.7, the scope of this thesis was three-fold: [1] match a synthesized spectrum to a measured absorption spectrum, [2] conduct scaling studies to design new experiments, and [3] synthesize new diagnostics of the photoionized plasma.

Despite the discrepancies in plasma temperature and absorption line wavelengths between the model and the experiment, the results of [1] demonstrate that our model still does a pretty good job of predicting the spectrum measured in the gas cell experiments. All strong lines for the ionization states in the measured spectrum also appear in our model, and our model also does a good job predicting some weaker features for the Li-like and He-like ionization states. Current deviations of the synthesized spectrum from the experimental spectrum (at least for the plasma temperature discrepancy) may arise from errors in experimental parameters we have for the viewfactor simulation, such as the albedo model for the surfaces in the experiment.

Next, using the same modeling procedure validated by [1], a scaling study was conducted for the particle density of the gas in the cell. For a Ne gas fill, the minimum density that will have measurable spectral features in absorption was found to be $\sim 7.5 \times 10^{16}$ cm^{-3}, which implies an ionization parameter for the plasma of ~ 70 erg cm s^{-1}. Future experiments could also utilize other gas fills for heavier elements (like Ar), which would achieve the same mass density for a smaller particle density.

Lastly, new spectral diagnostics of the photoionized plasma were synthesized in the form of time-resolved absorption and emission spectra. These new diagnostics can be used as a more stringent test of our spectral codes by allowing comparison between the model and the experiment for multiple times in the experiment and for multiple system parameters (temperature and ionization distributions). For future experiments similar to shot Z543, the synthesized spectra predict that the measured time-resolved spectra should show a weakening of Li-like lines in both absorption and emission and the strengthening of the Lyman α line in emission as time progresses.

7. Acknowledgements

REFERENCES

J. E. Bailey, D. Cohen, G. A. Chandler, M. E. Cuneo, M. E. Foord, R. F. Heeter, D. Jobe, P. Lake, D. A. Liedahl, J. J. MacFarlane, T. J. Nash, D. Nielson, R. Smelser, and W. A. Stygar. Neon photoionization experiments driven by Z-pinch radiation. *Journal of Quantitative Spectroscopy and Radiative Transfer*, 71:157–168, 2001.

D. H. Cohen, J. J. Macfarlane, J. E. Bailey, and D. A. Liedahl. X-ray spectral diagnostics of neon photoionization experiments on the Z-machine. *Review of Scientific Instruments*, 74:1962–1965, March 2003.

M. A. Liberman, J. S. De Groot, A. Toor, and R. B. Spielman. *Physics of High-Density Z-Pinch Plasmas*. Springer, 1999.

D. A. Liedahl, S. M. Kahn, A. L. Osterheld, and W. H. Goldstein. X-ray spectral signatures of photoionized plasmas. *ApJ*, 350:L37–L40, February 1990.

J. J. MacFarlane. VISRAD-A 3-D view factor code and design tool for high-energy density physics experiments. *Journal of Quantitative Spectroscopy and Radiative Transfer*, 81:287–300, September 2003.

J. J. MacFarlane, I. E. Golovkin, and P. R. Woodruff. Helios-cr, a 1-d radiation-magnetohydrodynamics code with inline atomic kinetics modeling. Technical report, Prism Computational Sciences, Inc., 2005.

D. Mihalas. *Stellar Atmospheres*. W. H. Freeman and Company, 1978.

J. Paradijs and J. A. M. Bleeker, editors. *X-ray Spectroscopy in Astrophysics*, volume EADN School X. Springer, 1999.

N. R. Pereira and J. Davis. X rays from z-pinches on relativistic electron-beam generators. *Journal of Applied Physics*, 64:1–8979, August 1988.

Prism Computational Sciences, Inc. *AtomicModelBuilder*, 2.6.0 edition. [http://www.prism-cs.com/Software/AtomicData/AtomicModelBuilder.htm].

Prism Computational Sciences, Inc. *HELIOS*, 2.1.0 edition. [http://www.prism-cs.com/Software/Helios/Helios.htm].

Prism Computational Sciences, Inc. *PROPACEOS*, 2.0.0 edition. [http://www.prism-cs.com/Software/PROPACEOS/PROPACEOS.htm].

Prism Computational Sciences, Inc. *SPECT3D*, 4.1.0 edition. [http://www.prism-cs.com/Software/Spect3D/Spect3D.htm].

Prism Computational Sciences, Inc. *VISRAD*, 4.0.0 edition. [http://www.prism-cs.com/Software/VisRad/VisRad.htm].

G. A. Rochau. *Radiative Transfer in Low-Density, Low-Z Foam.* PhD thesis, University of Wisconsin - Madison, 2003.

M. Sako, D. A. Liedahl, S. M. Kahn, and F. Paerels. The X-Ray Spectrum and Global Structure of the Stellar Wind in VELA X-1. *ApJ*, 525:921–934, November 1999.

N. S. Schulz, C. R. Canizares, J. C. Lee, and M. Sako. The Ionized Stellar Wind in Vela X-1 during Eclipse. *ApJ*, 564:L21–L25, January 2002.

R. B. Spielman, C. Deeney, G. A. Chandler, M. R. Douglas, D. L. Fehl, M. K. Matzen, D. H. McDaniel, T. J. Nash, J. L. Porter, T. W. L. Sanford, J. F. Seamen, W. A. Stygar, K. W. Struve, S. P. Breeze, and J. S. et al. McGurn. Tungsten wire-array Z-pinch experiments at 200 TW and 2 MJ. *Physics of Plasmas*, 5:2105–2111, May 1998.

This preprint was prepared with the AAS LaTeX macros v5.0.